Study of flow fields in mixing tanks with particles using CFD

Sergio Poveda Ruiz

Thesis for the degree of Master of Science in Engineering
Division of Fluid Mechanics
Department of Energy Sciences
Faculty of Engineering | Lund University

Study of flow fields in mixing tanks with particles using CFD

MASTER THESIS 2021

MASTER OF SCIENCE IN ENGINEERING. MECHANICAL ENGINEERING.

Sergio Poveda Ruiz ©
se0236po-s@student.lu.se

June 2021 , Lund

This degree project for the degree of Master of Science in Engineering has been conducted at the Division of Fluid Mechanics, Department of Energy Sciences, Faculty of Engineering, Lund University.

Supervisor at the Division of Fluid Mechanics was Professor Johan Revstedt.

Supervisor at Tetra Pak Processing Systems were Dragana Arlov and Fredrik Innings.

Examiner at Lund University was Professor Christer Fureby.

The project was carried out in cooperation with Tetra Pak Processing Systems AB.

Thesis for the Degree of Master of Science in Engineering

ISRN LUTMDN/TMHP-21/5482-SE

ISSN 0282-1990

Division of Fluid Mechanics

Department of Energy Sciences

Faculty of Engineering, Lund University

Box 118, 221 00 Lund

Sweden

www.energy.lth.se

Acknowledgement

This Master Thesis has been a challenge that allows to end this journey the best possible way. Multiple persons have helped me to overcome several problems that have existed during this time. Firstly, I need to thank Tetra Pak as a company for allowing the students to be part of these projects. These are demanding, but also are the perfect experience to understand how industry and business work. Thus, I need to thank my industrial supervisors at Tetra Pak Dragana Arlov and Fredrik Innings. Your advice and guidance has been extremely helpful. Thanks as well to Johan Revstedt, my academic supervisor for being always attentive and contributing with valuable expertise in CFD theory. Special and warm thanks to Konrad Jarosz and Mani Johannesson from Star-CCM+ support, for always responding my endless list of questions.

Finally, I would like to thank everyone who has been part of my life during my Master's Degree. Their unconditional support was, sometimes, the only motivation that pushed me forward in difficult moments.

Now, onto the next one.

Sergio Poveda Ruiz
Lund
June 30, 2021

Abstract

The demand of food products with particles has increased in the last decades. Among them, yoghurt with fruit pieces or cereals can be found. Thus, the food processing industry is facing important challenges to offer these products meeting the quality requirements. Tetra Pak creates then this project to research and increase the knowledge of how these fluid-particle interactions behave. The main goal of this line of work is to correctly create good mixing and thus, particle distribution. By doing so, the final product can have the correct amount of cereals within the yoghurt, for example.

This study develops a CFD methodology to predict the behavior of flows with particles. This methodology is applied on two production scaled tanks with different shape and stirrer geometries. Experiments are conducted on the tanks to obtain validation data to compare with the simulations. The study investigates the ways of modeling the stirrer prescribed motion (SM and MRF), and the use of RANS and URANS models to predict the flow behavior. The particle modeling is conducted by 1-Way Coupled Lagrangian Particle Tracking (LPT) and Discrete Element Modeling (DEM). The implications of this models are assessed.

The findings show that the turbulence model SST $k-\omega$ is able to model the flow behavior. The prescribed motion can be modeled using an initial solution computed by MRF and continuing the simulation using SM to capture some unsteadiness. The particle studies suggest that 1WC LPT is not fully recommendable when sedimentation exists. 1WC DEM results offer more physical results. However, none of them is fully capable to predict the results obtained in the experiments.

As a side goal, the two tank stirrers are assessed. The stirrers are named in this project *ViscoJet* and *Magnetic*. The ViscoJet presents both in the experiments and in the simulations lousy results. A lack of bottom-to-top movemente is predicted and therefore no good mixing and particle distribution are found. On the other side, the Magnetic stirrer creates better bottom.to-top flow field, but the particle distribution is still poor.

Keywords: solid-liquid mixing, particle suspension, aseptic tanks, stirrer geometries, flow fields, URANS, particle modeling, LPT, DEM.

Nomenclature

Acronyms

Abbreviation	Description
1WC	One Way Coupled
2WC	Two Way Coupled
CAD	Computer Aided Design
CFD	Computational Fluid Mechanics
DEM	Discrete Element Method
LES	Large Eddy Simulation
LPT	Lagrange Particle Tracking
MG	Magnetic (stirrer)
MRF	Multiple Reference Frame
PDE	Partial Differential Equation
RANS	Reynolds Averaged Navier-Stokes
RSM	Reynolds Stress Models
SM	Sliding Mesh
E-E	Eulerian-Eulerian
E-L	Eulerian-Lagrangian
VJ	ViscoJet (stirrer)
VOF	Volume Of Fluid
SST	Shear Stress Transport
CC	Curvature Correction

Latin symbols

Symbol	**Description**	**Units**
C	Constant	$[-]$
C_d	Drag coefficient	$[-]$
F_b	Body forces	$[N]$
F_c	Contact forces	$[N]$
F_d	Drag force	$[N]$
F_g	Gravity force	$[N]$
F_p	Pressure force	$[N]$
F_s	Surface forces	$[N]$
F_{vm}	Virtual mass force	$[N]$
H	Liquid height tank	$[m]$
k	Turbulent Kinetic Energy	$[m^2s^{-2}]$
Np	Power number	$[-]$
N_q	Flow number	$[-]$
N_{js}	Just suspended speed	$[-]$
Re	Reynolds number	$[-]$
Re_T	Tank Reynolds number	$[-]$
Re_p	Particle Reynolds number	$[-]$
V_t	Terminal velocity	$[m/s]$
d_p	Particle diameter	$[m]$
c	Impeller clearance	$[m]$
T	Tank diameter	$[m]$
u	Velocity	$[m/s]$
Δt	Timestep	$[s]$
N	Rotational speed	$[rad/s]$
Q_l	Impeller flow rate	$[m^3s^{-1}]$
L	Characteristic length	$[m]$
g	Gravity constant	$[ms^{-2}]$

Greek symbols

Symbol	**Description**	**Units**
ε	Dissipation rate of TKE	$[m^2 s^{-3}]$
μ	Dynamic Viscosity	$[kgm^{-1}s^{-1}]$
ν	Kinematic Viscosity	$[Pas^{-1}]$
ν_T	Eddy viscosity	$[m^2 s^{-1}]$
ρ_l	Fluid density	$[kgm^{-3}]$
ρ_p	Particle density	$[kgm^{-3}]$
σ	Constant	$[-]$
τ	Torque	$[Nm]$
ϕ	Variable	$[-]$

Index

Index of figures

Index of Tables

Chapter 1

Introduction

1.1 Background

The food processing industry has a clear objective: to transform primary food products into food for human consumption. This is achieved by a set of operations that include mechanical, thermal and chemical treatments performed in food processing lines. Tetra Pak is one of the biggest companies in this industry, manufacturing and developing process unit operations. With the possessed *know-how*, the company can suggest the customers the ideal equipment to obtain the desired final product. Tetra Pak business within the food industry, is oriented mainly towards the processing of dairy, beverages, plant-based products or other types of prepared food.

Different unit operations form a processing line. Figure 1.1 shows an example of a real line used for Quarg production. Among the necessary equipment, one of the most vital ones are the intermediate tanks. These tanks have the main function of storing the food temporarily before it continues along the line. Usually, these tanks must also preserve the food safety so aseptic conditions are guaranteed. Aseptic tanks prevent the product from being contaminated with unwanted microorganisms, by thoroughly sterilizing the tank using high temperature steam. Furthermore, after this sterilization, a slight over-pressure with sterile air is added in the tank, so no microorganisms from the outside can go in. The control of this inner pressure requires remotely controlled valves. Generally, these tanks are built in stainless steel, and contain an outside control panel so the user can accurately control the outflow, the pressurization and the steam for sterilization. The size of these tanks can vary but generally are within the range of $1m^3$ to $50m^3$. By using aseptic tanks, immediate advantages are presented, such as product loss reduction, energy saving and overall increased efficiency.

When the food product contains particles, extra equipment is needed in the tank. The general topology of these tanks is depicted in Figure 1.2, where one can see the vessel, and a stirrer. When the particles are more dense than the fluid, these sink and sediment at the bottom of the tank. This accumulation is undesired, since it makes the particle distribution inhomogeneous in the tank and increases the risk of uneven particle distribution during emptying. To prevent this sedimentation, the stirrer is placed inside the tank to continuously agitate the flow with particles. This agitation is designed to create a homogeneous suspension of the particles, achieving a homogeneous particle distribution when emptying. The position and geometry of the stirrer is interesting to study, since it changes the flow motion and

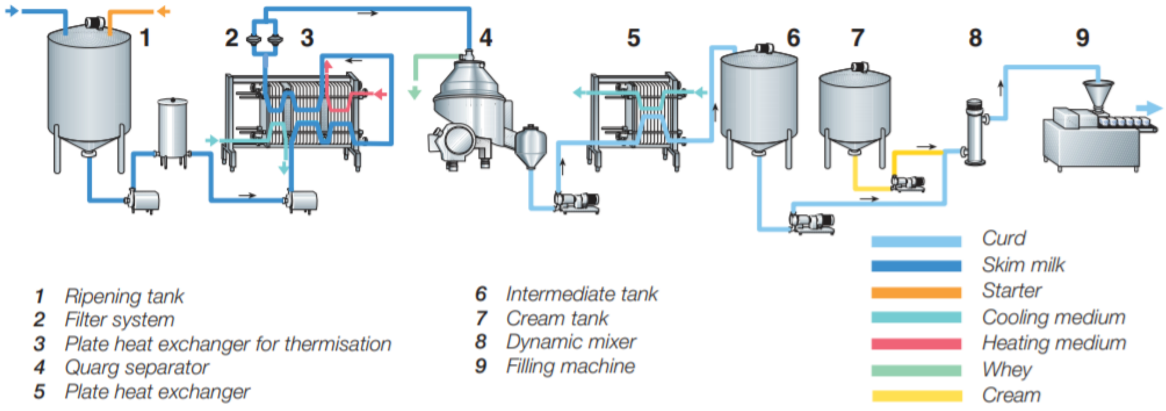

Figure 1.1: Processing line for Quarg production. [1]

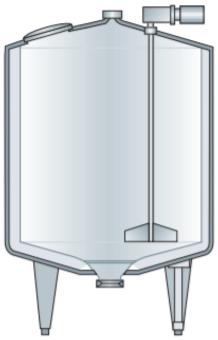

Figure 1.2: Intermediate storage tank with agitator. [1]

therefore, the final quality of the product.

For engineers, designing homogeneous conditions within the tank, is a really difficult task. In the food processing industry, Computational Fluid Dynamic (CFD) techniques can be used to model and predict the flow behavior. This, has been used for many years now due to its big utility when it comes to reducing the needed experimental trials. Shortly summarized, CFD methods solve fluid dynamic equations in a modeled reality to predict the behavior of the flow. With CFD then, the engineers are able to design correct solutions. One of the biggest advantages of this type of simulations is that allows to comprehend what is happening within the bulk of the fluid, in positions and with variables that are otherwise unreachable by experimental probing. This allows an enhanced understanding of the problem and thus, provides insights towards a better product and process design.

It is also possible to model flow with particles using CFD simulations. This is, however a substantially less developed topic. Predicting the trajectories and motion of the particles is, in general, computationally demanding. Multiple methods to deal with particles exist nowadays, making this possibility extremely interesting for companies and engineers aiming to reduce costly experiment tests and measurements.

1.2 Scope of the project

The aim of this thesis is to develop a CFD methodology that is able to predict flow fields, and particle distribution on production scaled tanks. A methodology is already available within Tetra Pak to handle these situations on small-scaled tanks. Therefore, this is used as the baseline for the future methodology and it is improved to include large-scale tanks.

Two different tanks were modeled, simulated and analysed. Both of them have a total volume of $12m^3$. The first tank is equipped with a stirrer called ViscoJet. This tank is thus, called on multiple occasions *"ViscoJet tank"*. The second tank is equipped with an off-centered, bottom-mounted stirrer. Since the impeller is moved magnetically, this tank is referred to, as *"Magnetic tank"*. Simulations are compared with data from experiments in each tank. These experiments investigate how the flow with particles behave within the tank.

Apart from the methodology development, both of the stirrers need to be assessed in terms of performance. Both simulations and experiments are used to evaluate their potential to create even particle distribution. The stirrer assessment is based on flow field analyses, and by observing how the particles are transported and suspended within the vessel.

Thus, by the end of this thesis, more knowledge on flow and particle distribution is expected. As well, two stirrers will be more understood. This allows Tetra Pak to suggest new tank configurations according to customer requirements.

1.3 Goals

The main goals of the thesis, according to the scope, are summarized in the following bullet points:

1. Develop CFD methodology for flow field simulations of production scaled tanks.
2. Develop CFD methodology for particle simulations of production scaled tanks.
3. Improve understanding of how stirrer and tank geometry affects the flow fields and particle distribution.
4. Assess the performance of two tank-stirrer geometries with respect the desired solid suspension.

1.4 Limitations

The scope of the project is delimited by the following points:

- The fluid is limited to water. No more viscosities are tested.
- The particles used are polymeric, assumed to be spherical. No food particles are tested nor modeled.
- No complex models that allow the correct simulation of the free surface are used. The liquid surface is assumed to be flat.

Chapter 2

Theory

2.1 Stirred tanks

Within the food processing industry, stirred vessels are a key component. A stirred tank is characterized by the vessel and stirrer geometries. Different configurations of these, create different distributions of the flow fields achieving different types of mixing. Despite all the research performed in the area, the theory is still in development and a wide extension of cases is based on empirical discoveries. Developing theoretic work in this area is a cumbersome process and continuous research is performed. In this section, the basic theory based on stirred tanks engineering is presented. Both empirical and theoretical analyses are discussed. Chapter 2.2 contains a section for the solid suspension and homogeneity analysis.

2.1.1 Influence of geometry

The design of the stirrer tank affects the flow behavior within the tank. Two basic components form a stirred tank: the tank, and the stirrer. Other additional elements can be part of the system, such as baffles and vortex breakers. In this section, the influence of geometry design is explored.

2.1.1.1 Vessel geometry

The flow in a stirred tank is dominated by the shape, size and position of the impeller, however, the tank geometry also has some influence. Figure 2.1 depicts some of the key parameters of the tank geometry such as the diameter (T) and the liquid height (H). The design of the tank bottom is also highly relevant. It has important implications for flow behavior and solid suspension lifting as seen in Section 2.2. The most common tank bottoms are the flat bottom, the ASME dish bottom and the shallow cone tanks, but other varieties may appear [2].

Another important point is how the liquid height affects the performance of the stirred tank capabilities in terms of mixing. A very high and narrow tank may be worse in liquid blending and an overall recirculation of the flow than a more *"low and wide"* tank. This is usually evaluated using the ratio liquid-height to tank-diameter (H/T). The optimum value[1] of this ratio for blending and solid suspension is normally about 0.6 to 0.7 [2].

---

[1] For minimum power consumption

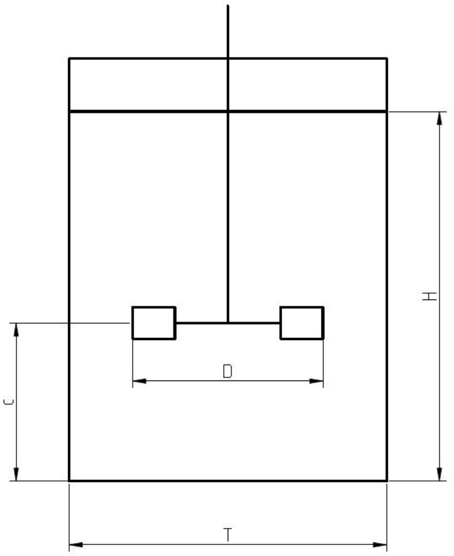

Figure 2.1: Basic parameters of a stirred tank.

2.1.1.2 Stirrer geometry

The design of the stirrer, deeply affects how the flow is disturbed due to the movement of the blades. Therefore, multiple variants of stirrers have been researched and are commercial nowadays. In this section, the most common categories are revised, without thorough details. Impellers can be divided into two general families: axial flow and radial flow impellers. The name is given after the main direction of the flow they produce within the tank. The stirrers analyzed in this thesis cannot be classified among any standard group. However, understanding how the standard stirrers perform is a key to identify similarities and improve the knowledge on the ones here treated.

When using an axial impeller, the main flow occurs parallel to the shaft i.e. the impeller axis. Some of the most known axial impellers are propellers and hydrofoils, and its effect on the flow field is depicted in Figure 2.2.

On the other side, the radial impellers have a flat or curved blade. Normally the discharge of the flow using these impellers is not purely radial due to the pressure difference along the blade height [2]. These, tend to pump upwards or downwards while discharging in a radial direction. A most common radial impeller is the Rushton turbine, stirrer with the blades plane parallel to the shaft direction, mounted on a disk. If the blades are located in another plane, inclined with respect to the shaft direction, the flow achieved is generally a combination of the two impeller families. Figure 2.2 depicts the typical discharge and flow patterns of the impeller types mentioned above. The flow describes a different path in all of the cases. When using an axial impeller, the flow is accelerated towards the bottom, where impinges and recirculates. Only one set of vortices are developed above the blades. With radial impellers, the flow impinges in the lateral walls due to the radial discharge. From that position, it can either recirculate in an upwards or downwards direction. Two sets of compartments of fluid are therefore created, the vortices developed in the tank bottom and the ones above the blades. Finally, the Pitch Blade Turbine provides an intermediate flow between both recently commented.

Each flow pattern may be useful for different applications. Liquid blending can be achieved with one circulation loop whereas for liquid-gas mixing may be more suitable to use a double loop using radial

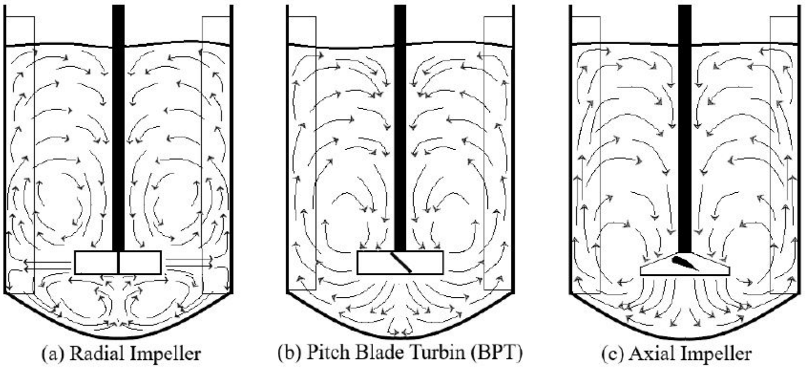

Figure 2.2: Flow patterns developed in a cross section for different impeller types [3]

impellers. In the specific case of solid sinking suspensions, as the one here treated, the most efficient technique is to provide a flow that impinges at the tank bottom, recirculating afterwards and creating particle lifting. In these cases is not uncommon to use a secondary axial impeller higher up in the tank.

2.1.1.3 Tank and impeller placement implications

The flow is strongly dominated by the position of the impeller within the tank. In the majority of the tanks, this location can be geometrically defined by the clearance and the offset.

- The clearance is defined as the height from the tank bottom to the impeller blades. See c in Figure 2.1.
- The offset can be seen as the horizontal distance from the position of the impeller to the center of the tank.

Both of these parameters affect the created loops in the flow. In Figure 2.3, examples of how the flow pattern may change by changing impeller placement are shown. In this project, the Magnetic stirrer researched is placed off-centered, and tilted. The implications of these characteristics on the flow fields are depicted in Figure 2.3, left.

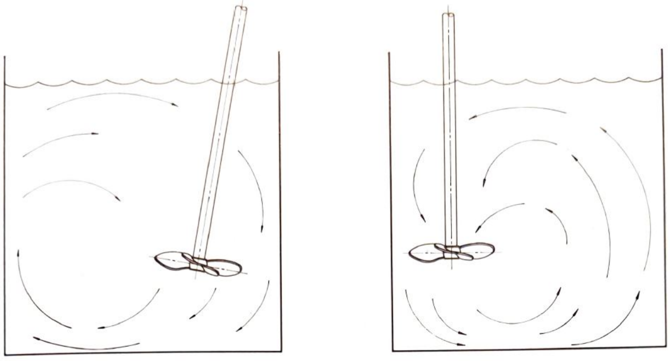

Figure 2.3: Effects of off-centered and inclined off-centered impellers [2].

It is important to remark however that the placement of an impeller is not only defined after the desired flow pattern. When solid suspensions are present and homogeneity is wanted, the desired flow pattern is combined with the emptying requirements. It is crucial to have good homogeneity when emptying the tank. Thus, the stirrer is normally located using a lower clearance than the optimum for flow pattern and power consumption. Having the stirrer far away from the bottom could achieve better homogeneity but when the liquid level falls below the impeller blades, the homogeneity decays[2] and the product has bad quality. To decrease this phenomenon, a couple of stirrers can be installed at different heights.

Multiple research have concluded some of the following tips [2]:

- When impellers are located too close to the tank bottom, the pumping capacities of the stirrer are throttled and the flow tends to develop a swirl.
- One impeller can usually handle liquid coverages from $0.5D$ to $2D$.
- If radial impellers are being stacked, these must be separated at least $1.5D$ apart.

Following these, the design of the tank-stirrer couple should go fulfill the desired characteristics. There are however, another set of elements that can be introduced to the tank so the quality of the flow pattern improves.

2.1.1.4 Influence of baffles and vortex breakers

Some other elements are often added to tank designs to enhance the performance. The most common ones are the baffles and the vortex breakers.

When the tank is cylindrical and has no additional elements, when stirred, a flow as the one in Figure 2.4 can be developed. A swirl is established, as the rotational component of the velocity remains untouched. Furthermore, due to the shaft spin, a suction starts to develop, creating a vortex of air that effectively reduces the liquid height in the center. This vortex deteriorates the homogeneity and mixing capabilities of the tank and can create mechanical instabilities.

This problem is commonly solved by adding baffles to the tank. The baffles are rectangular platens that are attached perpendicular to the tank walls and act as rotation momentum breakers. When a baffle is added, the flow moves from the one in Figure 2.4 to Figure 2.5, i.e. the baffles break up the swirl and the surface vortex is therefore strongly diminished.

Since the baffles also enhance the vertical fluid motion, mixing is improved. This effect can also be achieved with an off-centered stirrer but it requires more power for a similar mixing performance.

Another air vortex can appear when draining the tank. The movement of the flow trying to replace the already evacuated liquid, together with the Coriolis forces of the rotational fluid, makes a fluid vortex that travels down the shaft and in extreme cases can block the outlet nozzle [4]. This worsens the efficiency emptying, decreasing the product quality. To decrease this problem, vortex breakers are introduced. There are three types of vortex breakers, the cross-type, the disk-type and the combination of them (Figure 2.6). All of them are placed at the outlet nozzle, so the rotational momentum is broken and the emptying can be done safely.

---

[2] Note that no more agitation is proportioned.

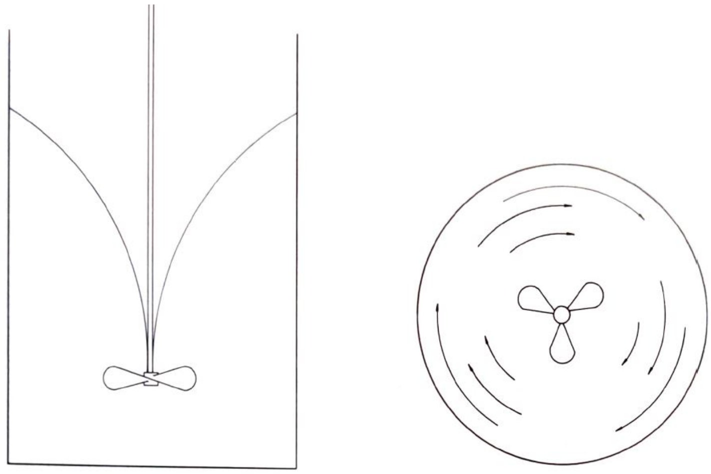

Figure 2.4: Swirling movement and suction of zone without baffles [2].

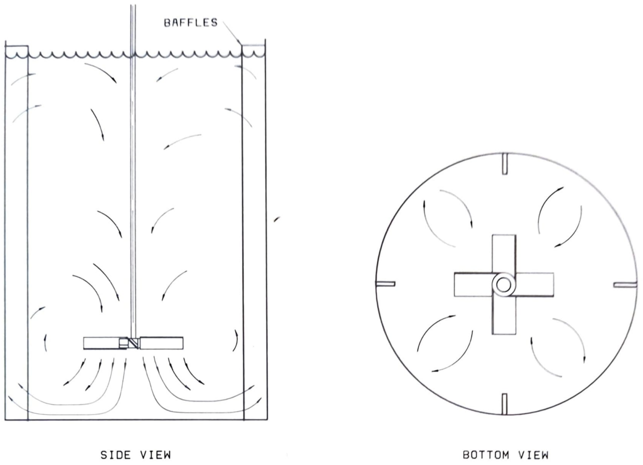

Figure 2.5: Effect of baffles on the flow pattern [2].

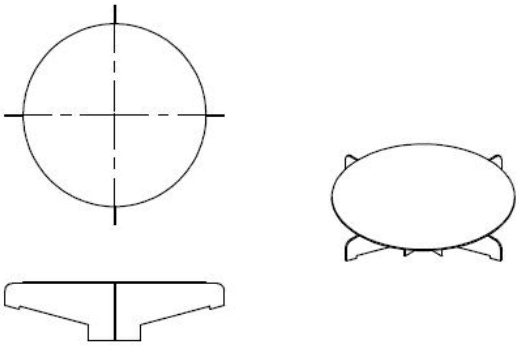

Figure 2.6: Design of a vortex breaker.

2.1.2 Relevant parameters

Normally, a set of parameters is used to characterize stirred tanks. These, are mainly related to the torque and mechanic capabilities of the stirrer together with the tank. Some of these parameters are explained in the following lines [5].

2.1.2.1 Power number

This parameter gives the power requirement needed to operate the agitator. It is defined as in equation (2.1) being P the power applied in the stirrer of diameter D, at an N rotational speed (in rps) agitating a fluid with density ρ_l.

$$N_p = \frac{P}{\rho_l N^3 D^5} \tag{2.1}$$

In the literature, is possible to find an extensive set of correlations to obtain experimentally this number. Lots of them, relating it with the Reynolds number [2].

When CFD's are available however, the power number can be calculated by obtaining the power of equation (2.1). This power (equation (2.2)) is no more than the product of the impeller speed and the torque delivered to the stirrer. The torque is easily calculated by computational software by integrating the pressure along with the blades.

$$P = 2\pi N \tau \tag{2.2}$$

2.1.2.2 Flow number

To evaluate the pumping capacity of an impeller, the flow number is used. It is described in equation (2.3) where Q_l is the flow rate that the impeller generates. This flow is derived by integrating the total outflow around the discharge region of the impeller.

$$N_Q = \frac{Q_l}{N D^3} \tag{2.3}$$

2.1.2.3 Reynolds number

One of the most recognized parameter in Fluid Dynamics, the Reynolds number is a dimensionless number that expresses the ratio of inertial and viscous subforces. It is normally used to define the fluid regimes, being valid to separate between laminar and turbulent. The known expression can be seen in equation (2.4) where L is the characteristic length, v is the fluid velocity and μ_l is the fluid dynamic viscosity.

$$Re = \frac{\rho_l L v}{\mu_l} \tag{2.4}$$

$$Re_T = \frac{\rho_l D^2 N}{\mu_l} \tag{2.5}$$

However, there are other definitions of Reynolds numbers. Equation (2.4) is transformed to equation (2.5) when applied to stirred tanks, for example. In this case, the rotational speed is used as velocity and the characteristic length of the tank is, its diameter[3].

---

[3] The squared diameter in the equation comes from substituting v for the peripheric velocity in the tank $v = ND$.

Finally, in solid suspensions, the Reynolds number of the particle can also be defined (see equation (2.7) in Section 2.2).

2.2 Solid suspensions

One of the most common processes in the mixing technology industry is the solid suspension. This can be defined as the phenomenon of solid particles being carried and suspended in a flow. In this case, applied within an agitated tank. Multiple aspects influence how the suspension behaves in the fluid. In this section, the fundamental theory existent regarding solid suspensions in stirred vessels is presented.

Among all the different types of solid suspensions, the one that adapts the aim of this study is solid dispersion. This process can be defined as the spreading of particles within a fluid by the action of an agitator to obtain a certain degree of homogeneity. Based on the solid-fluid density difference, this dispersion is obtained in a different way. Either the particles sink and the objective is to lift them, or the particles float and suction must be provided. The most common case, and therefore more studied, is the one where the particles settle i.e. particle density higher than liquid density.

2.2.1 Settling velocity of particles

When a particle is placed in a fluid, and its density is higher, it sinks. Furthermore, when the fluid is motionless, that sinking velocity will increase from the moment the particle is placed until it reaches a steady-state. This steady velocity is normally referred to as terminal velocity or free settling velocity. This condition appears when the buoyancy of the fluid and the drag forces acting on the particle balance each other [5].

Calculating the real settling velocity in an agitated tank is complex due to the necessary turbulent description. Therefore, the terminal velocity is often used to describe the solid suspension regardless of not being the real sinking velocity within the tank. Different studies have proven that, the real sinking velocity is a function of the terminal velocity.

Correlations exist for the terminal velocity, mostly for spherical particles. The most common in studies is present in equation (2.6) where g is the gravity, d_p is the particle diameter, ρ_s density of the particles, ρ_l liquid density and C_D is the drag coefficient. This correlation is valid for Newtonian fluids.

$$V_t = \sqrt{\frac{4g_c d_p \left(\rho_s - \rho_l\right)}{3C_D \rho_l}} \tag{2.6}$$

$$Re_p = \frac{\rho_l V_t d_p}{\mu} \tag{2.7}$$

The drag coefficient necessary to obtain the terminal velocity is function of the Reynolds number of the particle, that can be calculated as equation 2.7 shows[4]. Three different regimes exist:

- Stokes' Law regime. Laminar regime with $Re_p < 0.3$.
- Intermediate regime. $0.3 < Re_p < 1000$.
- Newton's Law regime. For turbulent regimes $1000 < Re_p < 35 \times 10^4$.

Correlations such as Schiller-Naumann yield the expressions for the regimes. Figure 2.7 shows graphically the regimes described.

---

[4] Since the equation has V_t in it, iterative methods may be used to obtain the terminal velocity.

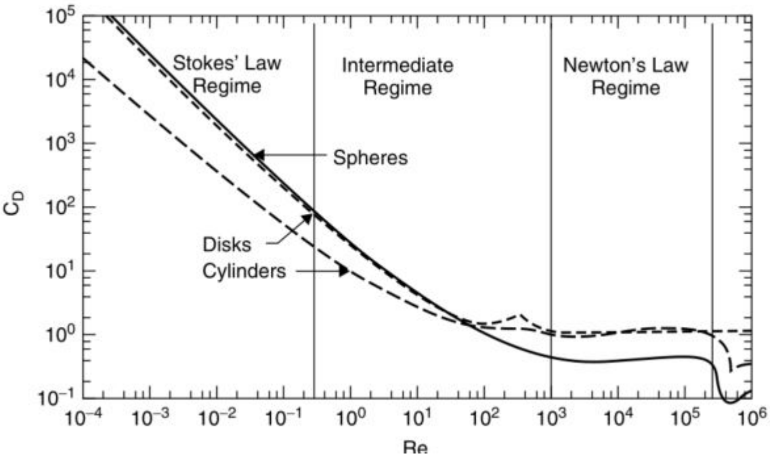

Figure 2.7: Drag coefficient evolution with Re_p [5].

On the other side, different terminal velocity correlations are derived empirically and can be found in the literature. This correlations aim to obtain the settling velocity by obtaining equations fitting important amounts of experimental data. Zhiyao et al. [6] present a study where different correlations are compared and a new and more efficient equation is derived. It can be seen in equation (2.8), where ν is the kinematic viscosity of the fluid, d is the particle diameter and d_* is defined in equation (2.9).

$$V_t = \frac{\nu}{d}{d_*}^3\Big[38.1 + 0.93{d_*}^{12/7}\Big]^{-7/8} \tag{2.8}$$

$$d_* = \left(\frac{(\rho_s/\rho_l - 1)g}{\nu^2}\right)^{1/3} d \tag{2.9}$$

This equation can be used for spherical solid particles with $Re < 2 \times 10^5$. In Section 4.1.1, this method serves as one theoretical reference for the experiments performed.

2.2.2 Basic condition for lifting

To get lifting of particles, the local bulk of fluid must have a higher vertical velocity than the settling velocity. This simple condition is exposed in equation (2.10). This condition is continuously evaluated in this project, to assess the solid suspension performance of the tanks.

$$V_{lift}/V_t > 1 \tag{2.10}$$

2.2.3 States of solid suspension

According to the distribution of the particles within the tank, the solid suspensions are widely classified into three different categories. These are:

- On-Bottom motion/Partial suspension. Visual observation shows that all the particles are moving around the tank bottom. This however, excludes different possible formations such as aggregation of particles close to the tank corners. This condition corresponds with Figure 2.8a.
- Off-Bottom or Complete suspension. Complete motion of all particles, where no particle remains more than 1-2s at the bottom base. This is normally identified as the *"just suspended"* condition,

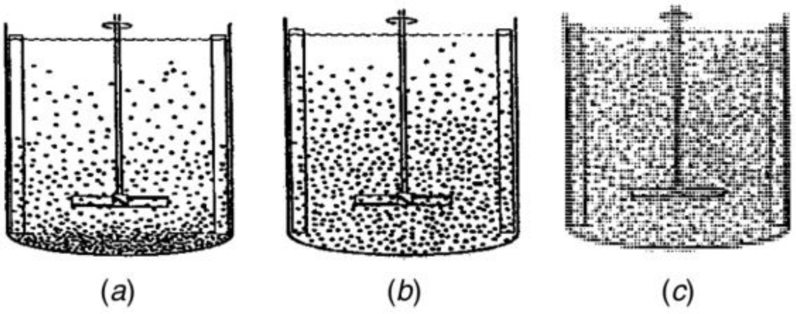

Figure 2.8: States of solid suspension based on particle distribution.

which is defined by the Zwietering correlation [5]. This level of suspension can be seen in Figure 2.8b.

- Uniform suspension. Particle concentration and distribution are almost uniform across the tank. This is depicted in Figure 2.8c. Further increases in agitator speed and power do not enhance the homogeneity levels.

The on-bottom suspension is normally not desired due to its bad homogeneity achieved. In general, the most desired state for industrial operations is the uniform suspension. However, this may be cumbersome to achieve due to the increase of power required to do so. Uniform suspension is usually considered to be achieved when the spatial variation in solid concentration is less than 5%. Due to the locally low axial lifting in the top of the tank this state is usually cumbersome to attain.

Different empirical studies have been made and the states can be illustrated based on Table 2.1. This table takes as a reference the case of On-Bottom motion, and it shows how both the speed ratio and the power ratio need to increase between the three states for different particle settling velocities[5]. Thus, when using particles with a settling velocity of 0.02-0.04 m/s, the power ratio would be 3 times more to get an off-bottom suspension, and 9 times to get a uniform suspension. The speed ratio would increase to 1.7 and 2.9 respectively.

Table 2.1: Power and speed requirements for different states [2, 5].

		Power ratio at settling velocity (m/s)		
		$0.08-0.3$	$0.02-0.04$	$5\times10^{-4}-0.003$
Suspension criteria	Speed Ratio	Difficult	Moderate	Easy
On bottom	1	1	1	1
Off-bottom	1.7	5	3	2
Uniform suspension	2.9	25	9	4

---

[5] In the original source (Oldshue[2]) the settling velocity is expressed in ft/min.

2.2.4 Off bottom suspension correlations

As discussed above, the off-bottom suspension state is key for the state definition of solid-liquid mixing. This state is normally defined by the condition of *just suspension* which expresses that no particle remains at the tank bottom more than 1-2s.

To achieve this state, a certain speed must be provided to the impeller, and the most common way to derive that speed is by using the Zwietering correlation. Obtained in 1958, the correlation is expressed in dimensional form in equation (2.11).

$$N_{js} = S\nu^{0.1}\left[\frac{g(\rho_s - \rho_l)}{\rho_l}\right]^{0.45} X^{0.13} d_p^{0.2} D^{-0.85} \tag{2.11}$$

where[6]:

- S is a dimensionless number function of the impeller, and the stirrer placement.
- ν is the kinematic viscosity of the fluid.
- X is the mass ratio of suspended solids to liquid, in percentage.
- d_p is the mass-mean particle diameter[7].

There are conditions, however where the exponents of the correlation need to change. Regions where the correlation is not reliable include solid loading below 2 vol %, high solids loading (more than 15 vol %) and high d_p/T. Some practical examples [5]:

- For particles bigger than 1mm in diameter, N_{js} seems unaffected by particle size.
- In turbulent regime, low effects of viscosity are expected, with studies showing that viscosity exponent could be between 0 and 0.2.
- Just suspended speed is easily achieved with dish-bottomed vessels than flat-bottomed ones. Conical bottoms are impractical.
- Just suspended speed is lower with smaller clearances.

2.2.5 Homogeneity in stirred tanks

To define how correct a solid suspension is, in terms of its mixing, different parameters can be used. Overall, the concept of homogeneity is the one that defines how the particles/fluid ratio is spread through the tank. When a tank is emptied, and therefore its content is driven somewhere else in the production line, the interest is to receive the most homogeneous concentration through all the emptying.

Evaluating the homogeneity of particles in stirred tanks is a cumbersome task. Several studies exist that deal with this topic but yet the matter is not completely defined. Along these lines, different parameters used to define the homogeneity are exposed.

---

[6] Every parameter that is not described, is in the glossary.

[7] For particles that change diameter/imperfections.

2.2.5.1 Cloud height method

When particles are stirred the flow carries them and if the correct conditions exist, these get lifted. The lifting of the bulk of the particles allows them to contact different turbulent regions and therefore enhances the mixing. Therefore generally, a stirrer that achieves better lifting and recirculation, achieves better homogeneity.

Using this simple concept, the Cloud Height (CH) approach is conceived. The CH is defined as the distance from the tank bottom to the steady height that the particles reach in the vessel. Below that height, the total quantity of particles in the system is found. Due to the unsteadiness of this height, which is affected by spatial and time variations, his approach is more typically a visual observation method, despite different existent correlations. As an example, if one observes Figure 2.1, it is possible to see how the CH is higher when the uniform suspension exists.

2.3 Computational Fluid Dynamics

2.3.1 Governing equations

Fluid flows can be described by the conservation laws of physics. This implies that the behavior of the fluid is correctly represented by a group of defined equations. As one can see in [7]:

- The total fluid mass must be conserved. This equation is known as the continuity equation.
- The change of momentum of a fluid element must equal the sum of forces on that element. Thus, the whole momentum must be conserved. This equation expresses Newton's second Law.
- The energy rate within the fluid must obey the First Law of Thermodynamics.

When the energy equation is not considered, the flow is governed by mass and momentum equations. These PDE's are often solved using Finite Volumes discretization techniques. In many applications, the fluid is considered to be incompressible (i.e. constant density) and Newtonian. When a fluid is Newtonian, the viscous stresses are linearly correlated with local strain rate. Applying these assumptions, lead the above-presented laws to the Navier-Stokes equations (2.12).

$$\begin{gathered}\frac{\partial u_i}{\partial x_i} = 0 \\ \rho\left(\frac{\partial u_i}{\partial t} + u_j\frac{\partial u_i}{\partial x_j}\right) = \rho g_i - \frac{\partial p}{\partial x_i} + \mu\frac{\partial^2 u_i}{\partial x_j \partial x_j}\end{gathered} \tag{2.12}$$

2.3.2 RANS equations

Turbulent flows are more difficult to describe since the big fluctuations cause the velocity and pressure fields to rapidly change. To make the problem possible to handle mathematically, the Navier-Stokes equations are often time-averaged. This idea uses the velocity decomposition concept into a mean and a fluctuating component.

$$\overline{u} = \frac{1}{T}\int_0^T u dt \tag{2.13}$$

As seen in [8], the mean velocity of a turbulent flow can be defined as equation (2.13) shows. Therefore, the fluctuating component would be nothing but the difference between the total velocity and the mean (time-averaged) one. When deriving the time-averaged equations and decomposing the velocity in these two parts, it is also important to remember that, by definition, the mean of the fluctuating part is zero.

$$u = \overline{u} + u' \tag{2.14}$$

Using then, the basic idea expressed in (2.14) and introducing it in Navier-Stokes equations (Eq. (2.12)), one derives the Reynolds Averaged Navier Stokes equations (RANS) (2.15).

$$\begin{aligned} &\frac{\partial \overline{u_i}}{\partial x_i} = 0 \\ &\overline{u_j}\frac{\partial \overline{u_i}}{\partial x_j} = -\frac{1}{\rho}\frac{\partial \overline{p}}{\partial x_j} + \nu \frac{\partial^2 \overline{u_i}}{\partial x_j \partial x_j} - \frac{\partial (\overline{u_i' u_j'})}{\partial x_j} \end{aligned} \tag{2.15}$$

The term $\overline{u_i' u_j'}$ is called the Reynolds stress tensor. This parameter needs to be modeled in order to close the system of equations and therefore, be able to solve it. Different theories and approaches have been derived to represent this tensor. The most common are the $k-\varepsilon$ model and the $k-\omega$ model, explained in Section 2.3.3. Both of them are based on the *"turbulent viscosity hypothesis"*. There are more complex approaches, based on the "Reynolds stress transport models" more accurate but also more computational demanding. By modeling the stress tensor, one closes the system of equations and thus it can be solved.

Due to the low computational resources needed by RANS models, the usage of them is widely spread through studies and researches. This is also increased based on the normal desire of the industry to obtain the mean behavior of the flow, without having an interest in understanding what is happening on every turbulent scale. The vast majority of articles and industry works are carried using RANS models. However, they also have their drawbacks, mainly based on the turbulent viscosity hypothesis, that makes them unsuitable in various situations.

In some occasions, a steady solution cannot be achieved when using RANS. This may be due to strong fluctuating or non-symmetrical flows. This can be resolved by using the time-accurate solution of the RANS equations, otherwise known as Unsteady RANS (URANS). This, is based on a triple decomposition of the time dependent variables. Each component of the decomposition is identified as average, periodic and turbulent. What they represent, can be observed in Figure 2.9, and equation (2.16) shows the decomposition. When using this approach, the sum of time-average and periodic components (known as coherent or ensemble-averaged component) is solved using turbulence closure models. The turbulent component as before, is modelled. Discern between the periodic and turbulent components is normally, a cumbersome task. This is a clear issue of scale separation, that can lead to wrong component definitions and thus, wrong fluctuations being resolved.

$$u = \overline{u} + u' + u'' \tag{2.16}$$

When flows need to be resolved with more accuracy, i.e. including the effect of certain small time or length scales, RANS and URANS equations may be the wrong approach, due to the time-averaging. To model this type of flows, one may use a different set of models such as *Direct Numerical Simulation (DNS)* or *Large Eddy Simulation (LES)*. These last two, resolve the velocity and pressure field in time and space, without the average that leads to RANS equations. DNS resolves directly the Navier Stokes equations with the trade-off of an extremely high computational power. Its usage is usually limited to

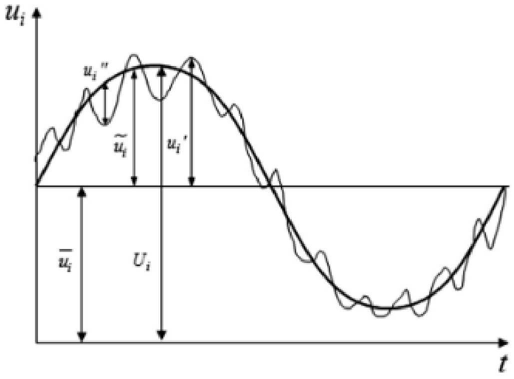

Figure 2.9: Triple decomposition for URANS method. [9]

cases with relatively low Reynolds numbers. LES on the other hand is a different model that resolves the large scales and models the small ones by using a spatial filtering.

2.3.3 RANS based turbulence models

In this section is discussed how the Reynolds Stress Tensor is modeled to correctly close the RANS set of equations and therefore obtain the mean flow quantities. Due to its high usage in the industry and research, different approaches exist to model this tensor, offering a wide set of possibilities. To understand each model with its benefits and drawbacks is crucial to understand and interpret the results obtained.

Most of the different models can be classified into two families [10]:

- Turbulent viscosity models.
- Reynolds stress transport models.

Eddie viscosity models.
Eddie viscosity models are based on the Boussinesq hypothesis, also called the turbulence-viscosity hypothesis. This theory assumes that the Reynolds-stresses can be calculated as in equation 2.17. One can see that the main assumption of the hypothesis is that the deviatoric (anisotropic) component of the tensor is proportional to the mean strain rate (S_{ij}) and a parameter called *turbulent viscosity* ν_T.

$$\overline{u_i' u_j'} - \frac{2}{3} k \delta_{ij} = \nu_T \left(\frac{\partial \overline{u_i}}{\partial x_j} + \frac{\partial \overline{u_j}}{\partial x_i} \right) = 2 \nu_T S_{ij} \tag{2.17}$$

The turbulent viscosity appears as a turbulent diffusion coefficient for momentum when mimicking molecular diffusion. The RANS models, model this parameter in different ways. To obtain the turbulent viscosity, one could use an algebraic equation to approximate the value, a PDE or a set of PDEs to solve new transport equations for variables not yet seen.

One good example of a 1-equation model would be the Spalart-Allmaras model, suitable for external aerodynamics applications. Among the 2-equation models, one can find the recognized $k - \varepsilon$ and the $k - \omega$ turbulence models. These, and their variations, are widely used in simulations of all kind. Its simplicity, combined with good results in lots of cases, make them extremely demanded. Due to the importance of the $k - \varepsilon$ and the $k - \omega$ models, a brief description of every important variation can be seen in the pages that follow.

However, the biggest drawback of all eddy viscosity models lies in the first assumption made. In general, assuming that the anisotropy is proportional to the mean strain rate limits the usage when the direction of the flow changes quickly. The Rapid Distortion Theory (RDT) proves, that the anisotropies are not proportional to the local mean strain rates [11].

2.3.3.1 k-Epsilon model

This 2-equation model, developed first by Jones and Launder [12], assumes that the turbulent viscosity can be calculated as in equation (2.18), being k the turbulent kinetic energy and ε the dissipation of the turbulent kinetic energy. C_μ on the other side, is a constant that takes the value 0.09. To obtain k and ε, the transport equation of each variable must be solved.

$$\nu_T = C_\mu \frac{k^2}{\varepsilon} \tag{2.18}$$

The transport equation for the turbulent kinetic energy is shown in (2.19) whereas the transport equation for the dissipation rate of the turbulence is obtained empirically and can be seen in (2.20).

$$\frac{\partial k}{\partial t} + \overline{u_j}\frac{\partial k}{\partial x_j} = P - \varepsilon + \frac{\partial}{\partial x_j}\left[\left(\nu + \frac{\nu_T}{\sigma_k}\right)\frac{\partial k}{\partial x_j}\right] \tag{2.19}$$

$$\frac{\partial \varepsilon}{\partial t} + \overline{u_j}\frac{\partial \varepsilon}{\partial x_j} = C_{\varepsilon 1}\frac{\varepsilon}{k}P - C_{\varepsilon 2}\frac{\varepsilon^2}{k} + \frac{\partial}{\partial x_j}\left[\left(\nu + \frac{\nu_T}{\sigma_\varepsilon}\right)\frac{\partial \varepsilon}{\partial x_j}\right] \tag{2.20}$$

Terms on the left-hand side can be spotted as the rate of change and the convection transport. On the right side, one finds the production, the destruction and the diffusive transport of both k and ε. To solve these equations, some different parameters like the production and the constants must be modelled.

This model has problems at handling the flow close to the walls, resolving vortexes, high pressure gradients, impinging and separated flows. However, a known revision of it makes it better especially when having strong streamline curvatures, due to the overprediction of TKE that the standard version offers in these cases. This revised model is known as the Realizable $k - \varepsilon$. To handle the walls, different wall functions can be used to enhance the behavior of the model.

2.3.3.2 Realizable k-Epsilon

As mentioned above, this is a revision of the original $k - \varepsilon$ that forces the Reynolds Stress Tensor to offer strict physical results.

The model differs from the original one mainly in the following ways [13]:

- New turbulent viscosity formulation, that makes the parameter C_μ limited by a formula, instead of being a constant.
- New transport equation for the turbulent dissipation ε, derived from an exact transport equation for the mean-square vorticity fluctuation.

2.3.3.3 k-Omega model

Being similar to the $k-\varepsilon$ model, now the specific dissipation rate is the second transport equation solved. The specific dissipation rate is defined in (2.21). The new transport equation is shown in (2.22). It can easily be obtained by introducing the previous expression in equation (2.20). This model was developed by Wilcox [14].

$$\omega = \frac{\varepsilon}{k} \tag{2.21}$$

$$\frac{\partial \omega}{\partial t} + \overline{u_j}\frac{\partial \omega}{\partial x_j} = C_{\omega 1}\frac{\omega}{k}P - C_{\omega 2}\omega^2 + \frac{\partial}{\partial x_j}\left[\left(\nu + \frac{\nu_T}{\sigma_\omega}\right)\frac{\partial \omega}{\partial x_j}\right] \tag{2.22}$$

This change makes the model better at handling vortices and it can also be used in the viscous sub-layer. Furthermore, it is also possible for it to handle adverse pressure gradients and the wall-boundary flow is well resolved if the case has a low Reynolds number. As a drawback, however, the model handles worse the freestream.

2.3.3.4 SST k-Omega model

This model is a good combination of the two models seen above. The SST[8] formulation can be used in the viscous sublayer i.e. near the wall without using dampening functions, behaving as the $k-\omega$ model. At the same time, when is further from the wall, in the freestreams, it acts as the $k-\varepsilon$. According to [15], this model has certain problems when dealing with stagnation regions and local strong accelerations.

One general problem of every 2-equation model is that they are poor at handling streamline curvature and rotations of the turbulent quantities. In general, the sensitivity of these models with these influences is lousy. Several solutions exist to increase that sensitivity, and one of them is the curvature correction. This solution includes a factor f_c that is implemented in the transport equation for the turbulent kinetic energy and incorporates effects related to strong curvatures and rotations [16]. Factor f_c can be calculated according to equation (2.23).

$$f_c = min\left(C_{max}, \frac{1}{C_{r1}(|\eta| - \eta) + \sqrt{1 - min(C_{r2}, 0.99)}}\right) \tag{2.23}$$

Where C_{max}, C_{r1} and C_{r2} are model coefficients and η is defined in equation (2.24). S_{ij} is the strain rate tensor, W_{ij} the absolute rotation rate and T a time-scale parameter.

$$\eta = T^2\left(S_{ij}S_{ij} - W_{ij}W_{ij}\right) \tag{2.24}$$

2.3.4 Large Eddy Simulation

This model is enclosed among the scale-resolving approaches. The idea behind it is to resolve the biggest turbulent length scales, and model the smallest ones, due to its high computational cost when resolving them numerically.

To achieve this idea, a space filter is used rather than the time average, as seen in the RANS equations. This filter cuts off the smaller length scales, and therefore the equations can be resolved without its effect. However, as previously mentioned, these scales must be modeled, mainly due to the importance that these have when dealing with near-wall flows or multiphase flows.

---

[8] Shear Stress Transport.

The basic equation for filtering an instantaneous flow variable, is expressed in equation(2.25), where $G(x, \Delta)$ is the filter function characterize by a filter width $\Delta = (\Delta_x \Delta_y \Delta_z)^{1/3}$ [17].

$$\tilde{\phi}(t, x) = \int \int \int_{\infty}^{\infty} G(x - x', \Delta)\phi(t, x')dx' \tag{2.25}$$

$$\phi = \tilde{\phi} + \phi' \tag{2.26}$$

With this filtering, each variable ϕ is decomposed into a filtered value $\tilde{\phi}$ and a subgrid value ϕ' which takes into account the small scales, and needs to be modeled. Different models exist for this task, being the most generic one the *Smagorinsky sub-grid scale model*[18], exposed in equation 2.27. In Section 4.2.1.2 LES is used to compare results with 2-eq RANS models, and the sub-grid modeling used is a variation of the one mentioned, but more complex. Developed by Germano et al. [19], this model is based on the *Smagorinsky model* but instead, it calculates the constant C with a local time-varying coefficient. This model is called *Dynamic Smagorinsky sub-grid scale model.*

$$\nu_T = C\Delta^2 \sqrt{\overline{S}_{ij}\overline{S}_{ij}} \tag{2.27}$$

2.3.5 Short review on turbulent models

Multiple studies have been carried during the last decades, modeling stirred tanks using CFD techniques. In the following paragraphs, a brief review of some of them is performed to understand which are the most widely used turbulence models in the literature and its implications.

In 2011, Singh [20] researched how different models predicted the flow behavior in a baffled tank with a Rushton turbine as stirrer. Among these models one can find the mentioned $k - \varepsilon$ and the SST $k - \omega$. It was concluded that every model predicted reasonably well the mean velocities but were poor at predicting the decay of mean radial velocity. Furthermore, $SSTk - \omega$ with curvature correction predicted well the turbulence generation and dissipation close to the impeller, in contrast with the $k - \varepsilon$.

Madhavi [21] in 2012, uses the standard $k - \varepsilon$ to model a stirred tank with solid suspensions. Conclusions lead to a correct prediction of the suspensions, capturing correctly the axial distribution of particles with different experiments being performed. The settling of solids was also correctly predicted.

Generally, standard $k - \varepsilon$ is chosen thanks to its simplicity, low computational costs and good agreement with experimental data, as shown in [22, 23, 24]. Other models such as RSM or LES are also widely seen whenever more accurate results are desired, especially when solving more frequencies and scales.

In previous works carried within Tetra Pak, it was seen that when modeling flow with particles, realizable $k - \varepsilon$ shown unphysical clusters of particles near the walls [25]. This was originally solved using RSM being computationally expensive. Research in [26] shows that SST-$k - \omega$ with Curvature Correction could solve this problem in a less expensive computation mode. This model is then, appropriated when dealing with multiphase flows (see Section 2.3.7).

2.3.6 Modeling prescribed motion in stirred tanks

If the products stored in the aseptic tank tend to separate phases or if good homogeneity is wanted when particles are involved, agitation must be provided within the vessel. This agitation is created using a stirrer that creates turbulence increasing the mixing capabilities.

When modeling this type of aseptic tanks, it is necessary to simulate the motion created by the stirrer. Different ways exist in order to do so. In essence, two regions are defined within the complete volume of the modeled tank. The first region is stationary and has no rotation added. The second one is the moving region, which tends to be close to the impeller. Separating these two, an interface exists acting as the connection between two regions, being responsible of the flow entities transfer. This separation can be seen in Figure 2.10, where the yellow-colored region is the spinning one.

Figure 2.10: Division in regions of the tank volume.

The moving region can be modeled using different approaches. Among them, two stand out above the others. These are the Multiple Reference Frame (MRF) and the Sliding Mesh (SM).

2.3.6.1 Multiple Reference Frame method

This approach applies a rotating reference frame to the spinning region. Based on it, a source term is added to each cell in the rotating domain. This source term simulates the rotation in the region, and that effect is propagated through the interface to the stationary region, transforming the local values from one frame to the other on a *cell-by-cell basis*[27]. One must remark that in this approach, the mesh is completely frozen. As the mesh is not moving, the position of the stirrer blades with respect to the stationary walls remains unchanged. Therefore, the final result obtained with MRF is dependant on the original position of the imported geometry. Different initial positions may lead to different final snapshots of the solution, being one of the major drawbacks of the methodology.

The MRF approach assumes that the volume assigned to the spinning domain has a constant rotational speed. By not having mesh motion, the steady state solution linked to that position of the stirrer can be computed. This makes the approach computationally cheap and, despite the limitations, accurate for several industrial problems. One big limitation is that, since the source term is added to every cell within the spinning region, no stationary walls can be located inside it. It can be used in baffled tanks, if the stationary domain can contain the baffles maintaining a good separation of the regions. The accuracy with MRF then, depends strongly on the impeller type and geometry.

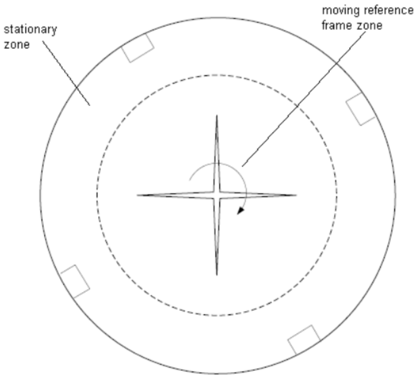

Figure 2.11: MRF approach. Region division and Reference Frame motion.

2.3.6.2 Sliding Mesh method

Opposed to the MRF, the Sliding Mesh (SM) [28] unfreezes the mesh and creates a real rotation in the model. This method (also called Rigid Body Motion), can offer transient results where the stirrer is spinning. Every timestep, the mesh rotates a designated quantity, sliding to a new position.

This methodology is computationally more expensive than the MRF but also more accurate. Since the mesh is moving, the interface computes interpolations between the interface to transfer the information between the regions. An example on the mesh movement can be seen in Figure 2.12

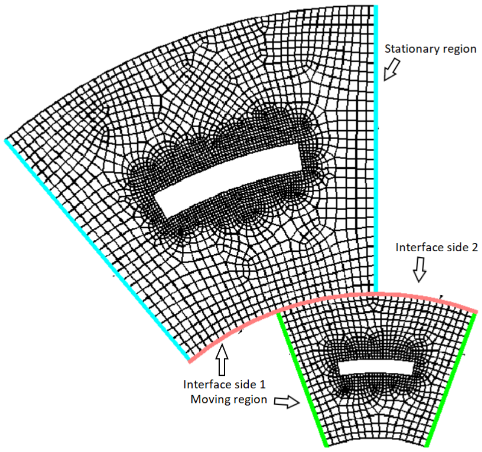

Figure 2.12: Sliding mesh approach. Displaced mesh example.

This method is thus, able to capture unsteady behavior of the flow, and therefore is not dependent on the original position of the stirrer. The set of conservation equations must be modified to compute the mesh motion, that use the grid velocity and the relative motion of the mesh with respect the stationary reference frame. These equations are [29]:

- Flow equations. Governing equations but adapted with the mesh motion i.e. including the abovementioned velocities.
- Conservation of space. Account for the changes of shape and position of cells.
- Grid flux calculations. Account the contributions of the mesh movement to the convective terms.

2.3.6.3 Short review on modeling prescribed motion

Multiple studies show the usage of MRF and SM when dealing with stirred tanks, since these are versatile, and ideal for rotating flows simulations. To understand how these are being used and also find flaws and strengths, a bibliography research is here presented.

De la Motte et al [30] in 2018 carry a research to identify the flow dynamics in a fully baffled stirred tank with two 4-blade Rushton turbines at different levels. To do so, CFD is compared with experimental data. For the CFD, both the MRF and the SM are simulated, and compared. In the results, it is possible to see how they both predict correctly the radial component and show the classical flow given by a Rushton turbine. However, the MRF is sensitive to the frozen position of the Rushton turbines. In comparison, SM predicts much better the behavior and specifically the vertical component and recirculation vortices.

On the other hand, the easiness of MRF and the low computational cost makes this model incredibly useful despite the flaws already explained. The potential then of this method makes it present in a big quantity of studies [24, 31, 32, 33].

Bibliography research shows that both MRF and SM are widely used in stirred tanks modeling.

2.3.7 Multiphase flows

When interactions of the flow with one or more extra phases exist, the flow is defined as a *multiphase flow* [34]. Normally, a phase is understood as a form of matter ie. solid, liquid or gas. However, when dealing with modeling, a phase can be considered every other entity present within the system that possesses its own physical properties. However, to be considered two independent phases, these must remain separated after mixing. Flows where the species are mixed at the molecular level, such as ethanol or water, are thus not considered multiphase flows.

The presence of particles in the flow, implies clearly a second phase. Solid particles are considered to be a dispersed phase, since they are present in disconnected regions of the space. Otherwise, the phase would be considered continuous.

The handling of a multiphase flow can be accomplished by defining:

- A particle modeling approach.
- A phase coupling. This defines the interactions between the phases.

Two main families of particle modeling approaches are used. The Eulerian-Eulerian (E-E) and the Eulerian-Lagrangian (E-L). Other advanced methods such as Volum of Fluid (VOF) exist, commonly used to resolve the free surface.

The E-E mixing models treat the fluid and the particle phase as continuous [35]. The same transport equations are thus solved and the particles are treated as a bulk, not individually. To be able to use this approach, the solid concentration must be high, allowing the continuum assumption. However, this is not normally the case for mixing tanks.

On the contrary, E-L mixing models treat the fluid as a continuous phase (Eulerian) , but the particles are considered a dispersed phase (Lagrangian). E-L formulation models the particle phase by solving a transport equation for the particle expressed in 2.28 [36]. This equation is known as the *particle equation of motion.*

Two E-L models are widely used to model particles in stirred tanks with low concentrations of particles. These are the Lagrangian Particle Tracking (LPT) and the Discrete Element Method (DEM).

2.3.7.1 Lagrangian Particle Tracking (LPT).

This method is designed for diluted concentration of solids. Thus, the particles are more affected by the continuous phase effects than by collisions with other particles.

The particles are solved in a Lagrangian framework, normally computed in statistical aggregations known as parcels. These parcels are followed across the continuum and commercial codes can save the track followed allowing the user to see the movement of the parcel.

Particle behavior is governed mainly by the Lagrangian conservation laws of mass and momentum. Boundary conditions must be specified to describe interactions with boundaries and between particles.

2.3.7.2 Discrete Element Method (DEM).

DEM is an LPT extension, where the particles interactions are modeled. The main difference remains in the inter-particle forces that are taken into account when solving the equations of motion. The particles are allowed to develop and overlap, changing the contact force calculated proportionally to that overlap. This methodology has higher computational costs, compared to LPT. Therefore, it is mainly recommended for dense particle flows, where the particle interactions need to be computed.

2.3.7.3 Particle equation of motion

To model the particle behavior, the particle equation of motion is solved, which computes the conservation of momentum for a particle (see equation (2.28)).

$$m_p \frac{d\mathbf{v}_p}{dt} = \mathbf{F}_s + \mathbf{F}_b \tag{2.28}$$

Where m_p is the particle mass, v_p the instantaneous velocity of the particle, F_s the forces acting on the particle surface and F_b the resultant of the body forces. The decomposition of these forces depends on the chosen specific particle models, which are seen in the following lines.

$$\begin{aligned} &\mathbf{F}_s = \mathbf{F}_d + \mathbf{F}_p + \mathbf{F}_{LS} + \mathbf{F}_{LR} + \mathbf{F}_{vm} + \mathbf{F}_c \\ &\mathbf{F}_b = \mathbf{F}_g \end{aligned} \tag{2.29}$$

The surface force ($\mathbf{F}_s$) is thus decomposed in the drag force ($\mathbf{F}_d$), pressure gradient force ($\mathbf{F}_p$), virtual mass force ($\mathbf{F}_{vm}$), lift forces ($\mathbf{F}_{LS}$, $\mathbf{F}_{LR}$) and the contact force ($\mathbf{F}_c$). The body force is simply, the gravity force ($\mathbf{F}_g$). All these forces are described in Appendix A.

Some forces can only be computed when using DEM, such as the contact force ($\mathbf{F}_c$). This force computes the interaction of two particles when they come in contact and collide.

Furthermore, particles can have orientations, and therefore equation (2.30) must be conserved, being $\mathbf{I}_p$ the particle moment of inertia, ω_p the particle angular velocity, M_b the drag torque and $\mathbf{M}_c$ the moment from contact forces. These forces are detailed in Appendix A.

$$\mathbf{I}_p \frac{d\omega_p}{dt} = \mathbf{M}_b + \mathbf{M}_c \tag{2.30}$$

2.3.7.4 Phase coupling

Phase coupling controls how the dispersed and the continuous phase affect and disturb each other [37]. Coupling affects directly how momentum and mass are exchanged between phases. Two main couplings exist, called 1-Way Coupled (1WC) and 2-Way Coupled (2WC).

Using 1WC, the continuous (Eulerian) phase is not influenced by the dispersed one i.e. the particles do not affect the flow fields. On the contrary, the continuous phase drives the particles, influenced by the existent fields.

On the other hand, using 2WC the particles affect the flow behaviour by exchanging momentum. That displacement is computed through the volume fraction of the Lagrangian phase. The volume fraction is defined as as the fraction of the local cell volume that is occupied by the phase. Equation (2.31) shows a simple way to calculate this parameter, where ϕ_c is the volume fraction and η is the ratio of volume occupied by the fluid phase to the total cell volume. In reality, this calculation is under-relaxed to promote stability.

$$\phi_c = 1 - \eta \tag{2.31}$$

By integrating the Lagrangian dispersed phase equations over a cell, the changes of momentum and mass are obtained. The sum of these changes for all particles yields the total exchanged quantities with the continuous phase.

When using 2WC and DEM approaches together, the particles interact between each other, and also affect the surrounding Eulerian phase. Thus, the net change of momentum can travel in all directions. This simulations are commonly known as four-way coupled (4WC).

Chapter 3

Methodology

3.1 Experimental studies

3.1.1 Settling velocity measures

Simple experiments are performed to measure the sinking velocity of the particles. The particles used in the experiments are named UBE PA6. These are polymeric particles with density $\rho_s = 1140 kg/m^3$ and an average diameter of $d = 2.6 mm$.

Complex procedures can be performed to accurately measure the settling velocity of particles such as holography. However, in this case, the experimental procedure is simpler and consists on a bucket filled with water, a chronometer and the particles. The experiment characteristics are described in Table 3.1.

Table 3.1: Settling velocity experiment characteristics.

Properties		**Value**	**Units**
Liquid (water)			
	Temperature	20	° C
	Viscosity	1	cP
Particles			
	Density	1140	kg/m3
	Diameter (average)	2.626	mm
Bucket			
	Liquid height	93	mm

The particles are carefully released on the free surface. The sinking time is measured and the average sinking speed can be calculated by using the widely known distance over time equation.

3.1.2 Homogeneity in tanks

To evaluate the homogeneity and particle distribution in the tanks considered, experiments are performed on them. The tanks are filled as in normal use, and after a certain time, where the flow has stabilized, particles are introduced by an opening in the tank ceiling. The tank is filled with water and the particle characteristics are the ones expressed in Table 3.1. A camera is filming for a long time, and then these videos can be analyzed to yield important information about the particle movement, cloud height and overall distribution.

The homogeneity was measured by using a methodology explained in detail in Lundström and Syrjä [26]. For this specific application, once the particles have been mixed for 30 minutes, with 30rpm of rotational speed, the tank is emptied. The content of the outflow is sampled with buckets every 2 minutes for half an hour. After, the sampling is made every 20 minutes.

The buckets are filled for approximately $2.5s$. For every bucket, the particles are strained and the weight of the particles and liquid is obtained. With that method, the concentration of particles can be obtained for different moments of the emptying. This is interpreted as a representation of the volume that is going out, and is compared with the CFD experiments.

The tank is emptied in a controlled manner, by choosing the outflow mass. This is possible due to a user-manipulated valve. The mass flow evolution is exposed 3.1a, where it can be seen that for the first half an hour, the mass flow is around $0.83kg/s$ increasing to $1.37kg/s$ afterwards. This mass flow creates the emptying described in Figure 3.1b, where an approximated time of 134min is required to completely evacuate all the fluid. From both of the plots presented, it can be seen that the density of samples is remarkably higher in the first interval, than in the second one.

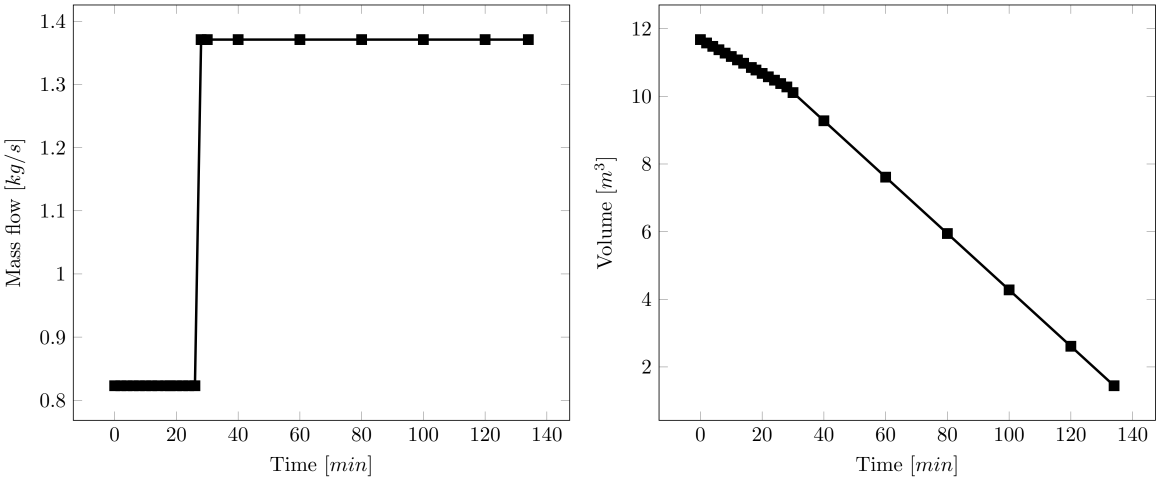

(a) Mass flow evolution.

(b) Tank emptying.

Figure 3.1: Homogeneity tests. Experimental procedure.

3.2 CFD Modelling - ViscoJet

3.2.1 Geometry model

A 3D model is created to represent the tank geometry. The modeling measures can be seen in Figure 3.3, giving the tank the expected approximated $12m^3$. The impeller has three conical mixing elements, that allow the flow to go through them. This stirrer has been designed by the company VISCO JET® Agitation Systems [38]. The three cones are 120º divided with each other so the whole space around the shaft is equally covered. Furthermore, the cones are slightly tilted down, which increases the mixing capabilities of the stirrer. The 3D model of the impeller represents accurately the real ViscoJet agitator used in the experiments. In Figure 3.2 two detailed views of the impeller are shown. The model assembled, with the shaft and the tank is depicted in Figure 3.3. The impeller diameter, not represented, is of $900mm$. The impeller is located at $146mm$ from the tank bottom. The most relevant measures are summarized in Table 3.2.

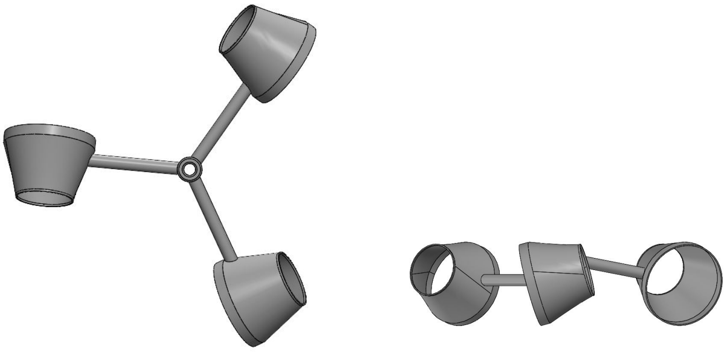

(a) View 1. **(b)** View 2.

Figure 3.2: ViscoJet stirrer detailed geometry.

Table 3.2: Measures of the $12m^3$ tank with the ViscoJet

Parameter	Value	Units
Diameter tank (T)	2.4	m
Height tank (H)	3	m
Diameter impeller (D)	900	mm
Clearance impeller (c)	146	mm

As mentioned in Section 2.3.6, to model rotations, two regions must be defined. A spinning region is created close to the cones enclosing them and also the closest proximity. The stationary region is the rest of the fluid volume, separated from the spinning region with the interface. Figure 3.4 depicts this separation.

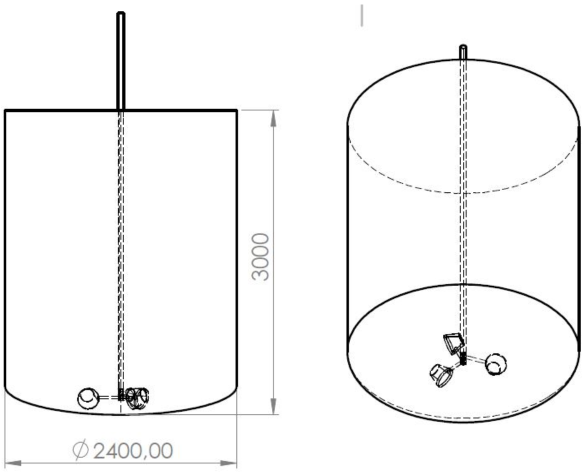

Figure 3.3: Model of the $12m^3$ tank with the ViscoJet stirrer.

Figure 3.4: Model used with the interface separating the two designated regions. Spinning section marked in yellow.

3.2.2 Boundary conditions

The spinning (rotating) region needs to define how the fluid interacts with the agitator walls and the bottom walls of the tank. Since both of them are solid material, the fluid cannot go through and therefore should be defined as *Wall.* Furthermore, the particles in direct contact with the wall act according to the adhesion law, which basically makes these particles travel attached to the wall. For taking into account this effect, the *No-Slip* condition is activated. To compute the rotation, the procedure is different depending on the approach used as one can see in Section 2.3.6. When MRF is used, a Rotational Reference Frame must be applied to the whole region. On the other side, when SM is the chosen methodology, a direct motion in Rotation form must be applied to the mesh. The rotation of this stirrer is defined as 30 rpm clockwise according to the shaft axis. Since this rotation is applied to the whole Spinning domain, the bottom wall included in this region must be locally specified to have no rotation[1].

The stationary region contains the free surface and the rest of the shaft and walls not included in the Spinning region. For the walls, the same principle is applied, so these are defined as *Wall, No-Slip.* In the free surface, interactions with air exist. To correctly model this behavior, VOF[2] should be used. To reduce the computational complexity of this boundary, the constraint is chosen to be as *Wall, Slip.* This

---

[1] Just for this boundary the local stationary frame is used.

[2] Volume Of Fluid, see Section 2.3.7.

is nothing but a rough simplification of reality that allows certain movement of the phases sliding with the false top wall. Since the air viscosity is low, it is more correct to model the wall with the zero-shear condition than with the No-Slip one. However, one must take into account that this tank, despite having the stirrer fairly low, is unbaffled. As can be seen in Section 2.1.1.4, this could produce an unsteady height of the free surface when creating a suction vortex. This condition must be chosen under caution since some errors may derive from it.

The stationary region includes as well, the rest of the shaft that was not considered in the spinning domain. These walls, have the *Wall, No-Slip* condition, but moreover, these walls should spin at 30rpm clockwise. Since no motion is assigned to the general domain, a Wall Relative Rotation is assigned to it, of exactly the mentioned rotation rate.

Finally, the interface is present as the layer that connects both domains and is in charge of transferring quantities between the two entities.

A summary of all the boundary conditions applied can be seen in Table 3.3.

Table 3.3: Boundary conditions of the ViscoJet model.

Region boundary		**Boundary condition**
Spinning		**MRF: Moving Reference Frame -30rpm.** **SM: Motion. Constant rotation rate -30rpm.**
	Agitator	Wall. No Slip.
	Bottom	Wall. No Slip.
Stationary		**Lab reference frame (stationary)**
	Shaft	Wall. No Slip. Wall relative rotation -30rpm.
	Top	Wall. Slip.
	Walls	Wall. No Slip.

3.2.3 Solver settings

The continua are created using the models shown in Table 3.4. With them, the general physics that rule the behavior of the system, are defined.

Three different turbulence models are set for this tank analysis. As can be seen in Section 4.2.1.2, a model sensitivity is performed with the aim to evaluate the different predictions that these could offer and therefore the robustness of the results with the choice of model. The chosen models were the Realizable $k - \varepsilon$ and SST $k - \omega$ both with Curvature Correction activated. Moreover, LES is also performed to include a more advanced model in the analysis.

As flow solvers, MRF is solved with Coupled Flow to get an initial solution of the fields. Once converged, this solution is used as a starting point for SM, which uses Segregated Flow. This choice of models was based on *Star-CCM+* recommendations. In general, coupled solver shown more stability when running MRF, which allowed a more smooth convergence of residuals, thanks to solving the equations simultaneously. On the other side, Segregated Flow shown good convergence when running SM having at the same time, less computational effort required.

Regarding the timestep for unsteady simulations[3], it is chosen as $\Delta t = 0.03$s, when using RANS turbulent models. This value is obtained based on the frequencies that wanted to be resolved. Since the highest

---

[3] When running Sliding Mesh.

frequencies were not interesting for the project, the timestep is set based entirely on the rotation rate of the stirrer and the desired sampling to resolve these frequencies correctly. In this specific case, 20 timesteps were desired for each blade passing. This way, the highest frequencies are not solved, and the scale separation issue present in URANS can appear to a lesser extent. On the other side, when running LES the choice of timestep has to reassure that the Courant-Friedrichs-Levi number is always below 1, to resolve correctly the small scales. The timestep is for this case reduced to $\Delta t = 0.002$ after a short set of tries and CFL monitoring.

Table 3.4: General models for the physics setup.

Physics		**Model**
Continua	Space	Three-dimensional
	Phase	Liquid
	Regime	Turbulent
	Density	Constant density (Water $\rho_l = 998kg/m3$)
Turbulence models		Real keps, SST kw CC, LES
Flow solver		MRF: Coupled Flow SM: Segregated Flow
Time Solver		MRF: Steady SM: Implicit Unsteady Real keps and SST-kw CC Timestep $\Delta t = 0.03s$ LES timestep $\Delta t = 0.002s$
Optional Models		Gravity Lagrangian Multiphase Discrete Element Model (DEM) for DEM simulations Multiphase interactions (DEM) Hertz-Mindlin contact

3.2.4 Particle settings

When simulation with particles are needed, new models should be included to predict the particle behavior. For this stirrer-tank combination, 1WC LPT and 1WC DEM are the cases run. This decision has been taken upon the conclusions seen in the previous thesis [26], where 2WC did not seem to enhance the predictions significantly.

In Table 3.5 the particle settings for the 1WC-LPT simulations are listed. The particles used model the ones used in the experiments and therefore, its characteristics are defined in Table 3.1. For the particle studies, a total number of 70.000 particles are injected.

Since no particle collisions are computed in LPT, there is no more necessary information related to particle interactions. The set of forces activated are also listed in Table 3.5. With them, the particle equations of motion will be solved.

The LPT is then compared with a second method, using in this case DEM. The coupling with the phase is still 1WC having then no interaction in direction particle-fluid. In Table 3.6 the settings for this case can be seen.

Table 3.5: ViscoJet model 1WC LPT physics setup.

1WC LPT	
Model	**Value/Type (if applicable)**
Lagrangian multiphase	Material particles
Solid	
Constant density	$\rho_s = 1140 kg/m^3$
Drag force	Schiller-Naumann
Pressure gradient force	
Shear lift force	Sommerfield
Virtual Mass force	
Turbulent dispersion	

Table 3.6: ViscoJet model 1WC DEM physics setup.

1WC DEM	
Model	**Value/Type (if applicable)**
Lagrangian multiphase	DEM particles
Solid	
Constant density	$\rho_s = 1140 kg/m^3$
Spherical particles	$d = 2.626 mm$
Drag force	Schiller-Naumann
Drag Torque	Sommerfield
Pressure gradient force	
Shear lift force	Sommerfield
Spin Lift force	Sommerfield
Virtual Mass force	
Turbulent dispersion	

3.2.5 Stopping criteria

The stopping criteria control how the running of the simulation behaves. Monitoring how the residuals or different engineering parameters such as torque converge, is what lately defines whether a solution is correct. The stopping criteria are set to fulfill that task.

To control the solution convergence, the criteria exposed in Table 3.7 are set.

The residuals monitored are the continuity error and the Specific Dissipation Rate (Sdr). Generally, the criteria are more flexible for unsteady cases, so a subtle increase can be seen in the abovementioned table.

Table 3.7: Stopping criteria set for the simulations.

Monitor	Type	Value	Logical rule
Continuity	Minimum	MRF: 1×10^{-5} SM: 5×10^{-5}	And
Sdr	Minimum	MRF: 1×10^{-3} SM: 5×10^{-3}	And
Torque	Asymptotic	1.00×10^{-3}	And
Maximum inner iterations (unsteady cases)	[-]	70	Or

Apart from the residuals, some engineering variables must be monitored, to reassure that the parameters of interest are also at a correct error level. In this case, the engineering variable to monitor is the torque. Setting the criteria specified in Table 3.7, this parameter is forced to converge within every time-step. In Figure 3.5 one can see how the convergence is achieved for every set of iterations.

Figure 3.5: Torque convergence with the set stopping criteria.

3.2.6 Post-processing

Along with the domain, different probes are situated to post-process information during the simulation run, and after its ending. These probes must be located strategically, to capture the desired effects and behavior correctly and not miss important information.

The tank equipped with the ViscoJet stirrer is completely symmetric and therefore axisymmetric flow is expected. Due to these special conditions, the total amount of probes is reduced to a few sections and planes, being able to understand from them the behavior of the whole domain. In Figure 3.6 different lines and points used for monitoring variables are represented. As can be observed, both the lines and the points are located in the cross section plane, and discretizing the domain height. With these divisions, the flow fields of interest can be tracked.

When dealing with particles, the analysis is based on identifying how these solids are dispersed across the domain. To understand how homogeneous the mixture is, the height distribution of particles is monitored. To correctly do this, the domain is divided in sections where the particles will be counted and compared with the fluid volume. This division can be seen in Figure 3.6c.

(a) Horizontal lines. Green $0m$. Blue $0.55m$. Red $1.35m$. Purple $2.8m$. Origin at impeller height.

(b) Points. Height of points correspond to lines.

(c) Fluid volumes division for particle analysis.

Figure 3.6: Probes for post-processing.

3.2.7 Mesh

To solve the PDE[4] seen in Section 2.3, the model is discretized in time and space. In this section the mesh that subdivides the domain in elements is analyzed.

For the tank equipped with the ViscoJet, a mesh sensitivity is performed in Section 3.2.8. With it, the independence of the results with the mesh is under inspection. Four different meshes are studied. The general settings of them are defined in Tables 3.8 and 3.9. All four studied meshes share the same default settings due to multiple findings in the previous thesis at Tetra Pak. The mesh is polyhedral, with prism-layers to resolve correctly the flow close to walls. As a general setting, five prism layers are chosen for the whole domain. The parameter called *Base Size* defined in length units, is a characteristic dimension that serves as a reference. Most of the refinements and controls are relative to this value and thus, by changing this Base Size, the mesh is parametrically affected.

However, to increase the accuracy of the overall iteration performance, different refinements are included

---

[4] Partial Differential Equations.

Table 3.8: Default controls of meshing.

Default control	Mode	Value
Base size	-	(*Case dependent*) m
Target surface size	Relative to base size	100%
Minimum surface size	Relative to base size	10%
Number of prism layers	[-]	5
Prism layer total thickness	Relative to base size	17.86%
Maximum Tet Size	Relative to base size	60%

Table 3.9: Local refinements of the mesh.

Surface	Local refinement	Mode	Value
Agitator	Prism Layers	[-]	5
	Target Surface Size	Relative to base size	10
Shaft	Prism Layers	[-]	5
	Target Surface Size	Relative to base size	10
Free surface	Prism Layers	[-]	3
	Target Surface Size	Relative to base size	50
Interface	Prism Layers	[-]	0
Walls	Prism Layers	[-]	2
	Target Surface Size	Relative to base size	50

in the meshing process. Every important surface is refined according to its requisites. The agitator and the shaft, due to its production of turbulence, are refined to have a smaller targeted surface size. The prism layers are kept to five. On the other side. The wall proximities are also refined, being the targeted surface size a 50% of the specified base size. It is remarkable as well that the interface is set to remove the general prism layers. Since it is a virtual wall, no prism layers are of interest near that boundary.

Having then, every refinement and default control scaled with the base size, the abovementioned four meshes vary precisely that parameter. The different chosen Base Sizes can be seen in Table 3.10 together with the total amount of cells. On the other side, the different meshes in a cross section of the model are exposed in Figure 3.7, where is possible to see how the cells increase significantly.

Table 3.10: Meshes used in the ViscoJet analysis

Mesh	Name	Base Size [m]	Number of cells
1	Extrafine	0.033	7M
2	Fine	0.05	4M
3	Coarse	0.075	2M
4	Extracoarse	0.2	1.3M

The main objective of this mesh sensitivity analysis is to understand the minimum number of cells that allow a good trade-off between computational time and results accuracy. Optimizing the mesh is one of the key steps when modeling due to its significant benefits in time-saving and error avoiding.

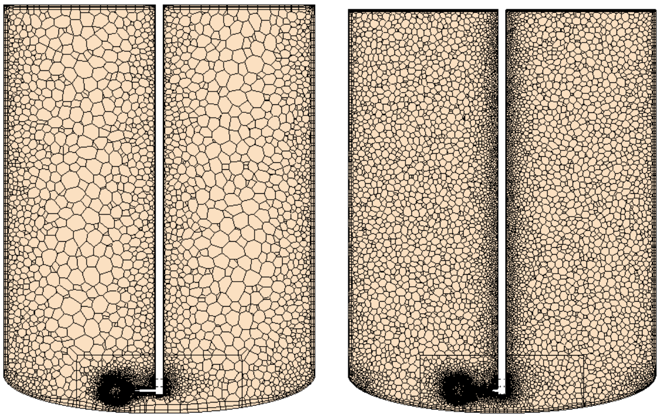

(a) Extra-coarse. **(b)** Coarse.

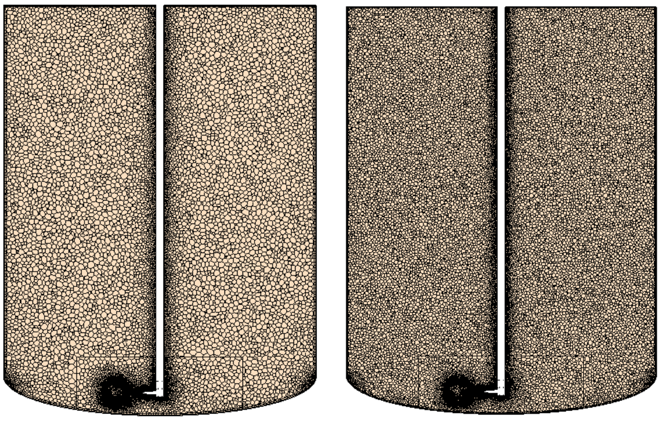

(c) Fine. **(d)** Extrafine.

Figure 3.7: Mesh sensitivity analysis. Meshes used for the ViscoJet tank.

3.2.8 Mesh sensitivity analysis

A mesh independence analysis is performed to select the best configuration of base size. The variation in base size changes the overall density of cells in the mesh. By varying this density, there is a clear change in resolution accuracy since different length scales can be resolved. The meshes tested have been presented in the previous section, exposed in Table 3.10.

SST $k - \omega$ is used as turbulence model. As explained in Section 3.2.3, a first steady solution is obtained by the MRF approach using the Fine mesh. This solution, is used to initialize the fields in every mesh presented in Figure 3.7. Therefore, the initial solution is always common for every tested mesh. The unsteady is run until the transient is determined to be over and the steady predicted by SM is reached.

To determine the mesh independence, the velocity fields and the torque are monitored and compared. This set of parameters define correctly the prediction of the flow fields and the physics within the tank. The obtained steady magnitude velocities are compared in a different set of horizontal lines (presented in Figure 3.6) for every mesh. These results are presented in Figure 3.8. On the other side, the torque evolution during the transient is also checked and its result, for each mesh, can be seen in Figure 3.9.

The velocity magnitude figures present in Figure 3.8 suggest relative mesh dependence. The predicted magnitude velocities along the lines match substantially well, but some differences exist. The flow field obtained is certainly homogeneous, not existing big difference in velocity profiles or absolute values of the

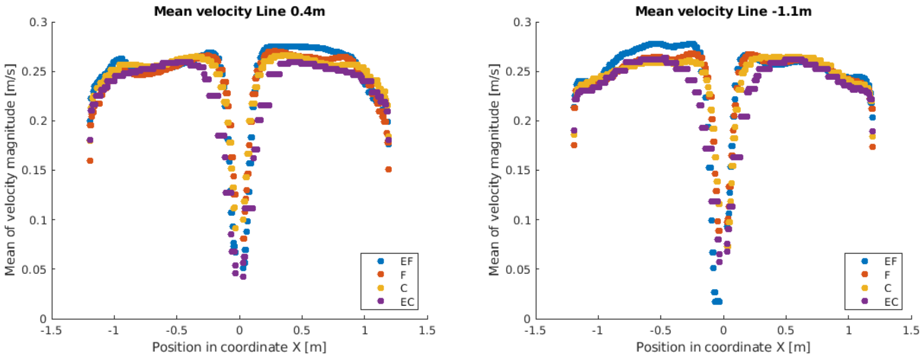

(a) Upper line. 2.8m. **(b)** Mid-Upper line. 1.35m.

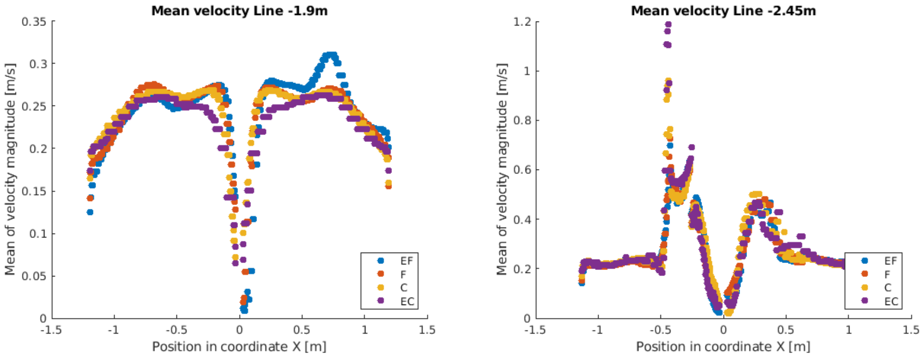

(c) Mid-bottom line. 0.55m. **(d)** Impellers-bottom line. 0m.

Figure 3.8: VJ Mesh sensitivity analysis. Velocity magnitude along horizontal lines.

velocity for the upper part of the tank. Thus, top left and top right figures are resembling. The flow gets more disturbed in the lower parts of the tank. Velocities are slightly over-predicted with the *Extra-fine* mesh, compared with *Fine* and *Coarse* ones. Elseways, the *Extra-coarse* mesh shows generally a lower velocity gradient in the shaft surroundings as well as a lower overall speed. Figure 3.8d shows that the flow is highly disturbed due to the cone effect of the stirrer. All of the meshes seem to predict correctly its effect since the matching of the lines is remarkable.

The torque evolution shows additionally, correct performance of every mesh. The transient compared shown in Figure 3.9 exposes how close the predicted steady value is, between the tested meshes. In this case, however, a considerable deviation can be seen when using the *Extra-coarse*. It must be mentioned that no fully stable solutions are achieved, since the flow seems to present low frequency unsteadiness. A simple average of the torque time series is presented in Table 3.11, together with the difference with respect the *Fine mesh*. Extra-Fine and Fine meshes are relatively close, whereas Coarse and Extra-Coarse are driven towards the 3% difference.

Table 3.11: Average torque and difference with the Fine mesh.

Mesh	Torque average (Nm)	Difference (%)
EF	-14.94	1.1%
F	-15.10	0.0%
C	-15.57	3.1%
EC	-15.70	3.9%

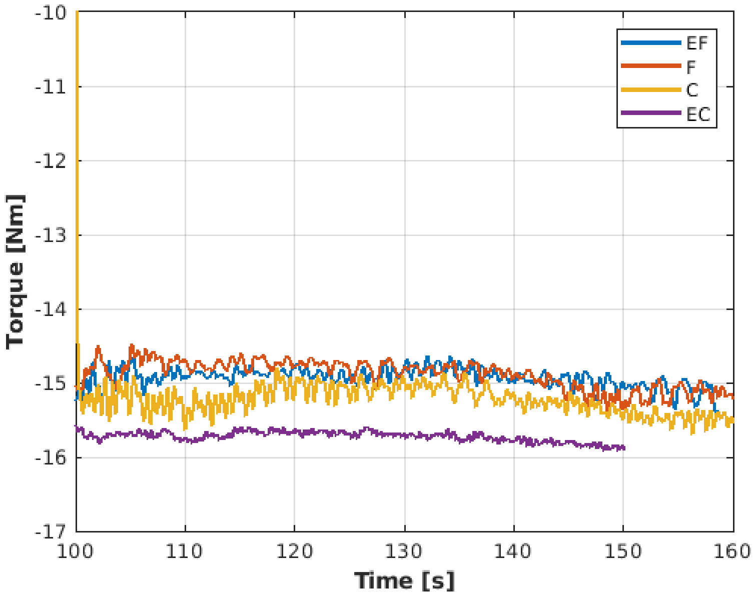

Figure 3.9: Torque transient for different meshes.

The obtained results, show an overall good performance of every mesh. Not high variations are observed in any of the cases, predicting almost equally the velocity profiles and the torque. However, when choosing the most suitable one, different appreciations must be discussed.

The Coarse and Extra-Coarse torque results from Table 3.11 suggest that these are not the best choices. Fine and Extra-Fine on the other hand, are closer and thus, more interesting to use. However, observing the velocity profiles there are no significant differences on the Coarse and the Fine mesh performances. The torque change thus, is not changing the field predictions to high extent. The Extra-Coarse mesh shows more deviatoric results both in Figures 3.8 and 3.9.

Based on the previous discussions, **the Coarse mesh is used in the simulations**. This, due to its good predictions of the velocity field, despite the small difference in torque; and also the reduced number of cells.

3.3 CFD Modelling - Magnetic

Together with the ViscoJet, another tank-stirrer combination is used for comparing methodologies and overall results. This tank presents a complete different topology. The stirrer is located at the bottom with an offset. The stirrer type is smaller and thus requires a higher rotation rate.

In this section, the CFD model for this tank-stirrer is detailed and the settings specified in Star-CCM+.

3.3.1 Geometry model

The second tank analyzed has the same total volume, $12m^3$. However, the tank geometry is slightly different, shown in Figure 3.11. This tank has lowe height but is wider, having therefore, a more *squared* T/H ratio. The bottom is more curved, with a higher elliptic minor radius. The stirrer in this case, is located off-centered tilted with a certain angle. Figure 3.10 depicts the magnetic stirrer geometry.

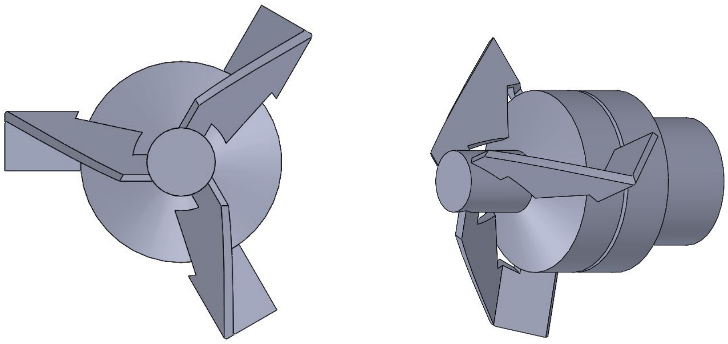

(a) View 1. **(b)** View 2.

Figure 3.10: Magnetic impeller detailed geometry.

Figure 3.11 shows the most important magnitudes defining the tank and stirrer location. To model motions, two regions are created. A spinning region models the rotation created by the impeller and thus the geometry encloses the impeller and its closest fluid volume. Then, an interface connects the spinning region with the rest of the volume, which is stationary. In Figure 3.12, both the regions can be seen.

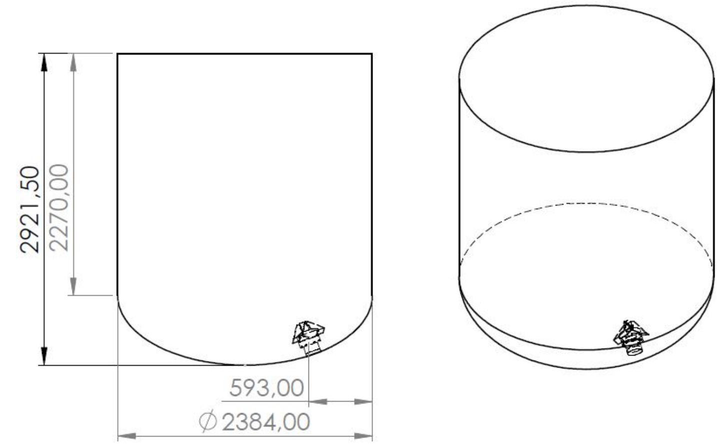

Figure 3.11: Model of the $12m^3$ tank with the Magnetic stirrer.

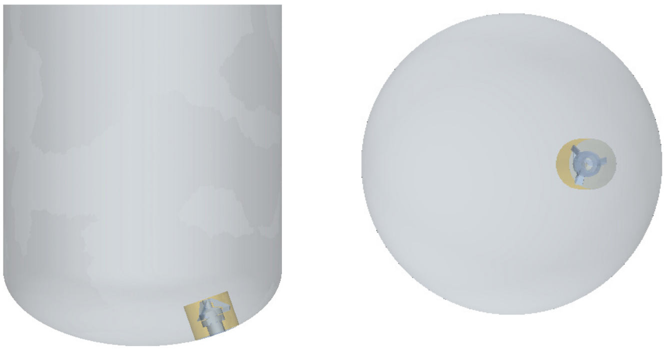

(a) Frontal view. **(b)** Superior view.

Figure 3.12: Regions defined for the Magnetic tank model.

3.3.2 Boundary conditions

Every boundary of the regions defined requires a constraint for the equations to be solved. These conditions, define the physics of the model. Since two domains exist, different constraints must be defined for each, according to the number of boundaries that are enclosed. In Table 3.12, every boundary is defined.

The stationary region includes the free surface boundary, and the tank walls. As can be seen in Section 3.2.2, the wall is normally modeled as *Wall, No-Slip* based on the adhesion law. The free surface on the other side, is approximated as a *Wall, Slip* so the boundary is simplified and more complex models such as VOF are not required. This solution is a rough approximation, and assumes that the free surface is steady and has no important motions.

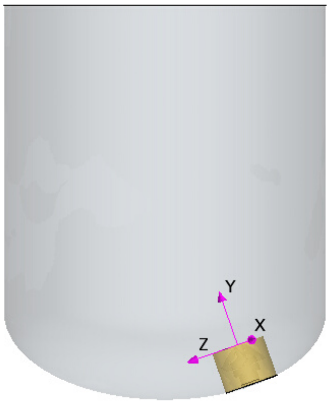

Figure 3.13: Coordinate system used to model the motion of the Spinning domain.

For the spinning region, a Moving Reference Frame rotating clockwise at 240rpm is set for the MRF studies. To achieve the correct motion of the system, another Reference Frame is created located as in Figure 3.13. This frame, can be rotated around the Y axis to correctly spin the domain. On the other side, a motion with the same rotating rate is specified in the SM cases. Since the whole domain has a defined motion, the remaining part of the tank wall enclosed by the spinning region has, apart from the *Wall, No-Slip* condition, a Local Stationary Reference Frame, that prevents it from rotating. Finally, the agitator is considered as a *Wall, No-Slip*.

Table 3.12: Boundary conditions of the Magnetic model.

Region boundary		Boundary condition
Spinning		**MRF: Moving Reference Frame -240rpm.** **SM: Motion. Constant rotation rate -240rpm.**
	Agitator	Wall. No Slip.
	Bottom	Wall. No Slip.
Stationary		**Lab reference frame (stationary)**
	Top	Wall. Slip.
	Walls	Wall. No Slip.

3.3.3 Mesh

The domain is subdivided in elements where the equations are solved. For the analysis of this tank, two meshes are used, where the principal difference is the base size of the cells and therefore the total number of elements. This is outlined in Table 3.13. The type of mesh is polyhedral since its usually more efficient in terms of convergence time and robustness. Prism layers are active to resolve the near wall flow.

The meshing is carried with the settings shown in Tables 3.8 and 3.9. These settings are applied to the ViscoJet tank and the Magnetic Tank.

A fine mesh is used to compute the flow fields. On the other side, for particle analysis, to reduce the computational time, the mesh is coarsened by increasing the base size. Both of the meshes can be seen graphically in two cross sections of the tank represented in Figure 3.14. The base size that parametrically scales the refinements and cell size is exposed in Table 3.13, where the total number of cells is also shown.

Table 3.13: Mesh characteristics for the Magnetic tank case.

Mesh	Name	Base Size [m]	Number of cells
1	Fine	0.050	3.4M
2	Coarse	0.075	1.1M

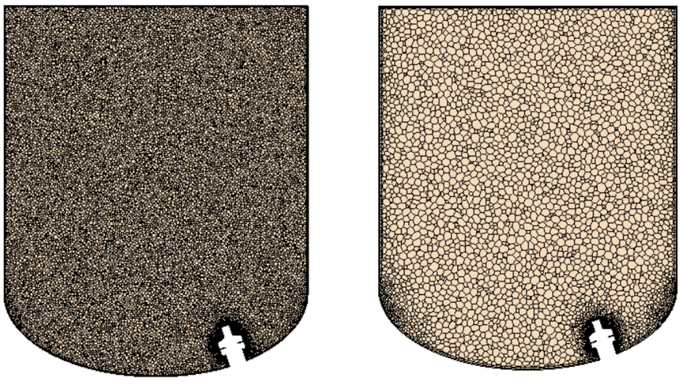

(a) Fine mesh. **(b)** Coarse mesh.

Figure 3.14: Meshes used in the Magnetic Tank analysis.

3.3.4 Solver settings

The solvers activated to simulate the correct physics, are exposed in Table 3.14. The majority of the models activated are common with the ViscoJet case[5] since the fluid and the particles introduced are the same.

However, since the stirrer spins at a higher rotation rate, the timestep to capture the blade frequency had to be decreased. By using 20 samples of each blade passing, the timestep is set to $\Delta t = 0.004$s. Furthermore, Segregated Flow behaved erratically in this case, so the SM cases are solved using Coupled Flow.

The findings seen in Section 4.2.1.2 for the ViscoJet tank, together than in previous thesis [26] helps with the choice of the turbulent model. Thus, the SST $k - \omega$ with Curvature Correction is the model selected.

The methodology followed computes an initial steady solution for the fields using MRF. Then, a transient is run switching to SM in order to understand the unsteadiness of the flow, if existent. Once the flow fields are known and identified, simulations of particles are carried to see the performance of this stirrer in mixing.

Table 3.14: Physics for the Magnetic tank cases.

Physics		Model
Continua	Space	Three-dimensional
	Phase	Liquid
	Regime	Turbulent
	Density	Constant density ($\rho_l = 998 kg/m3$)
Turbulence models		SST kw CC
Flow solver		MRF: Coupled Flow
		SM: Coupled Flow
Time Solver		MRF: Steady
		SM: Implicit Unsteady
		SST-kw CC Timestep $\Delta t = 0.004s$
Optional Models		Gravity
		Lagrangian Multiphase
		Discrete Element Model (DEM) for DEM simulations
		Multiphase interactions (DEM) Hertz-Mindlin contact

---

[5] See in Table 3.4.

3.3.5 Particle settings

The method followed with particles for this tank is completely analogous to the ViscoJet one. Therefore, particle characteristics can be observed in Table 3.6 for DEM ones.

The same number of particles, 70.000, are injected in the tank, to compare truthfully the differences, since both of the tanks have the same volume of fluid approximately. Hence, mass/volume fractions can be used in that analysis.

3.3.6 Stopping criteria

The stopping criteria selected can also be seen in Table 3.7. The objective of this criteria is to stop the inner and global iterations when the solution is converged. Some residuals controls are set to know that the governing equations are being correctly resolved. On the other side, the torque convergence is also checked each timestep.

3.3.7 Post-processing

The post-processing of the magnetic tank is performed in a similar way to what can be seen in Section 3.2.6.

The most relevant part for the analysis are the two sets of planes represented in Figure 3.15c. In this case, due to the stirrer position, the flow is not expected to be axisymmetric, and thus, a set of 90° planes are used. One crosses through the impeller section.

To perform the particle axial analysis, a set of volumes is defined, discretizing in height the tank (Figure 3.15d.). This is used to evaluate the particles inside each volume section, compared with the total number of particles injected.

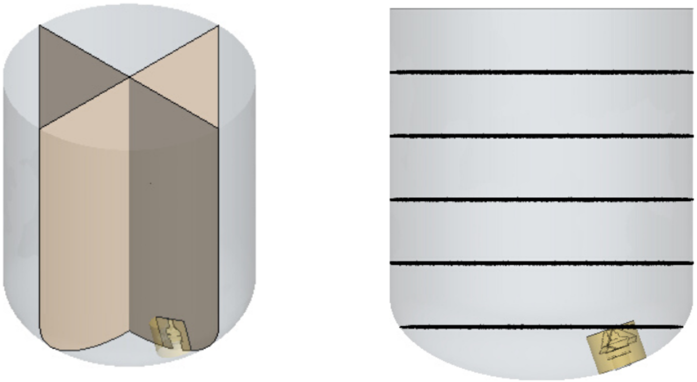

(a) Planes. Cross section and side section.

(b) Volume sections.

Figure 3.15: Probes for post-processing. Magnetic tank cases.

Chapter 4

Results and discussion

4.1 Experimental results

4.1.1 Settling velocity of particles

According to the procedure explained in Section 3.1.1, the particles are released from the liquid surface of a bucket filled with water and the settling speed is measured.

To compute statistical variations and also prevent important errors in the final value, the procedure is repeated fourteen times. The average and the standard deviation of the samples are specified in Table 4.1. The settling velocities obtained in each try are present in Table C.1, found in Appendix C.

To validate the accuracy of the measure the empirical equation (2.8) developed by Zhiyao et al. [6] is used to compute a value for comparisons. The empirical predicted value and the one obtained in the experiments are compared in Table 4.2. The difference between them is relatively small.

Table 4.1: Experiments for settling velocity calculation results. Average value and Standard deviation.

Average	Standard deviation	Units
0.061	0.008	m/s

Table 4.2: Experimental settling velocity against Zhiyao et al. [6] equation.

	Experiment	Zhiyao	Units
ws	0.061	0.059	m/s
Difference	-	3.0	%

4.1.2 Homogeneity test for the ViscoJet tank

The methodology explained in Section 3.1.2, is performed. The obtained mass concentration of particles across the volume can be derived. Each sample represent the evacuated volume in the experiment. The obtained mass concentration is after normalized with the total mass concentration. Figure 4.1 depicts the abovementioned normalized mass concentration. In the first set of samples, the normalized mass concentration is around 45%, as seen in the Figure 4.1. After approximately 10% of the tank volume emptied, a clear drop in concentration exist, from 60% to 0%. This infers that the totality of the particles allocate in the lower 10% bottom of the tank.

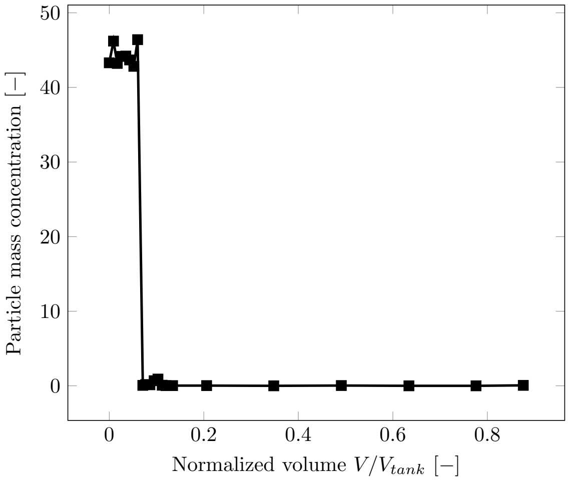

Figure 4.1: Homogeneity in the ViscoJet tank. Experimental results.

4.2 ViscoJet CFD results

4.2.1 Flow fields

In this section, the flow field simulations are showed. By flow field simulations, it is implied that no particles are included in this analysis. These set of cases aim to determine how the stirrer acts, possible lifting capabilities and also evaluating the quality of the methodology used.

4.2.1.1 MRF predictions

To characterize the fields, and understand how the particles can be lifted, the velocity contours are of interest. Since the tank is unbaffled, the flow is assumed axisymmetric and therefore the fields are presented in a cross section.

In Figure 4.2 four contour plots are presented, exposing the velocity components. The range is clipped when necessary to correctly identify structures. The stirrer seems to create a discharge flow radially, according to Figure 4.2b. This discharge flow does not impinge in the wall but stops and moves axially in a lifting structure visible in red designed zones in Figure 4.2a. Analyzing these structures, some part of the flow creates a pair of vortices at the tank bottom, whereas the rest recirculates in an upper and bigger vortex close to the shaft. This structure is close to reach the free surface, and near the shaft proximities, a big region with negative velocity is found. The absolute value of the velocity in these recirculations is, however fairly low, and poor lifting is expected. Green areas in the axial and radial figures show the lack of movement existent in these velocity components. Comparing the axial field with the obtained

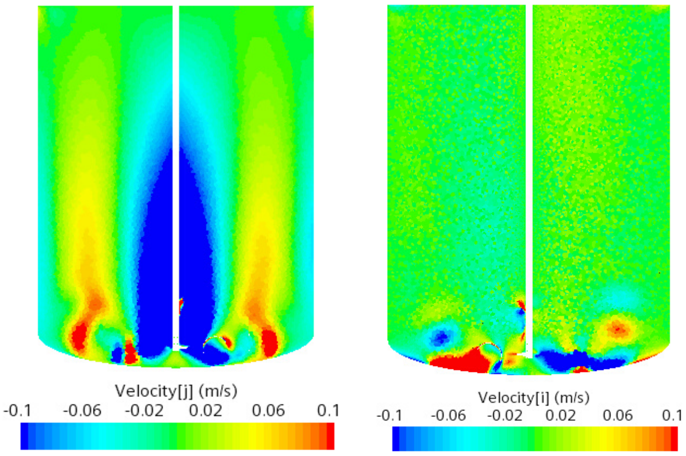

(a) Axial velocity field. **(b)** Radial velocity field.

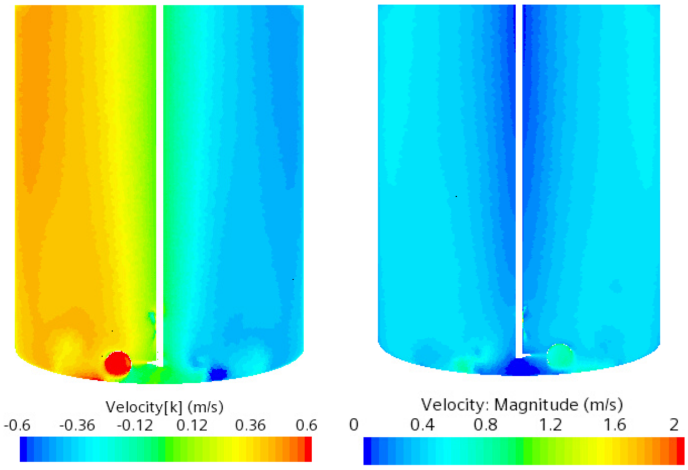

(c) Tangential velocity field. **(d)** Magnitude velocity field.

Figure 4.2: Velocity flow fields in cross section. MRF results.

settling velocity of the particles[1], only red and orange colors in the axial velocity map can produce lifting, according to equation 2.10 and the experimental settling velocity of $0.061 m/s$.

Figure 4.2c shows the tangential component of the velocity. From the range chosen to represent the field, a 5:1 ratio is observed when comparing rotation with axial and radial recirculation. A big general swirl is predicted along with the complete height of the tank. The flow distribution also shows movement close to a solid body rotation, where the velocity increases radially and decreases near the wall interaction zone.

---

[1] See Section 4.1.1

4.2.1.2 SM: Turbulence model analysis

To see the dependence of the results with the chosen turbulent model, a model sensitivity analysis is performed. To do so, the same case is run with different models, and the final steady result is compared.

Three different models are used, two RANS based models (the Realizable $k-\varepsilon$ and SST $k-\omega$) and LES. The purpose of using LES lays in using a model that numerically resolves the large scales.

The initial solution from Section 3.2.8 is also used here as the starting point for the transient calculations. The three models are then run until the fields and engineering variables stabilize. These stabilized solutions are then compared to evaluate the impact of the turbulence models.

The velocity field results can be seen in Figure 4.4. The three velocity components are observed in a cross section of the tank. Realizable $k-\varepsilon$ shows a radial discharge flow that does not impinge in the tank walls. That can be seen in the first row of Figure 4.4. The solution obtained is fairly similar to the one seen in the original MRF result, used as initialization of the fields[2]. Thus, the axial structures are similar, with the two lobes of positive flow that is collected near the shaft and recirculated downwards. On the radial contour, the two clear vortices at the bottom can be observed. For the tangential map, the field shows an increasing rotation in the outer domain. The speed increases radially when moving away from the shaft. The wall effect seems to decelerate the flow tangential velocity.

SST $k-\omega$ shows different set of flow fields. The discharge flow impinges the wall and moves upwards. At some point, the flow detaches from the walls and moves towards the center. The central region has a low negative velocity, recirculating down the flow. Above the detached stream, two counter vortices seem visible in the radial contour. The tangential flow field shows a higher increase of speed close to the shaft, but then that speed is stabilized and slowly increases until the wall effect plays a role, when it decreases again.

After the differences seen using the RANS models, LES is used. The results can be seen in the last row of Figure 4.4. More motions, as expected, are captured using this approach. From axial and radial contours, many small recirculations can be seen. However, the axial field seems to present the jet impinging the wall and the flow upwards at the wall. The match in this flow field between SST $k-\omega$ and LES suggests a correct prediction. The tangential field however is remarkably different from the one predicted by the RANS models. A vortex of high speed exists from top to bottom of the tank and it is created immediately above the cones of the stirrer. This high speed of the vortex is decreased radially until it reaches the walls.

The effect of this vortex is also reflected in the torque. Since the gradient of pressure from both sides of the cones is lower due to this vertical vortex, the required torque must also be lowered, see Figure 4.3.

The big difference in shapes and magnitude of the tangential component is reflected in the overall velocity magnitude. To see the gap between the LES predictions, and the ones with RANS models, Figure 4.5 is obtained. The velocity magnitude profiles along four horizontal lines[3] are presented. Essentially the results could be classified according to the slope existent in radial position, for the upper lines (Figures 4.5a and 4.5b). Meanwhile Realizable $k-\epsilon$ shows a positive slope from the shaft to the walls, the SST $k-\omega$ has a quasi-plateau and the LES presents a negative slope, decreasing dramatically the speed from the already commented vortex. The order of magnitude of the RANS models results are similar and comparable whereas the LES ones are more than doubled. It must be mentioned that the cone behavior is similarly captured with every model, as seen in the bottom right picture.

The results show then, an important dependence of the model chosen. To evaluate the validity of the solutions, and to choose one model to complete the simulations, a brief comparison with experimental

---

[2] See Section 4.2.1.1.

[3] Explained in Section 3.2.6.

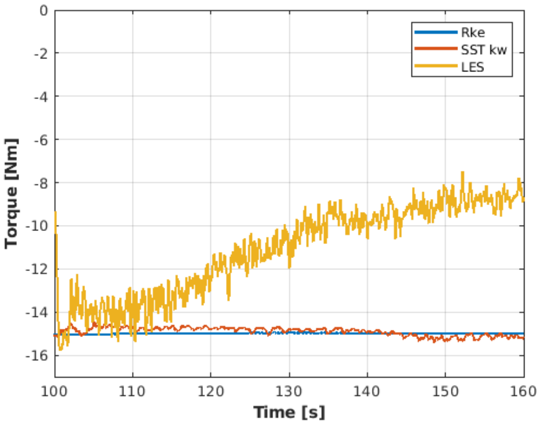

Figure 4.3: Torque comparison. Model sensitivity analysis.

data is performed.

Using a video recording of the experiment, some particles that travel onto the liquid surface are measured in length. This length is obtained when the video is paused, being it function of the camera shutter speed and the real speed of the particle. By seeing the relative difference in length between two particles traveling at different radius, the velocity profile from Figure 4.4a. can be validated.

All these calculations and validations can be found in the Appendix C.2. The relevant results are presented in Table 4.3. Distance 1 represents an inner radius whereas Distance 2 is closer to the walls. From the table, one can see that the difference in the average length of the travelling particles is small. The standard deviation of all population of the 20 samples taken show overlap. This means that the linear velocity on the free surface stays relatively constant.

Table 4.3: Results from free surface analysis.

	Distance 1 mm	**Distance 2 mm**
Average	7.7	6.1
SDEV	1.0	1.3

These results yield thus, that the profiles given by Realizable $k-\varepsilon$ and LES are not possible (see Figure 4.5a.). The first, predicts a radial increase of the velocity. The second, presents a peak of velocity close to the shaft that decelerates fast. On the other side, SST $k-\omega$ predicts almost a fairly constant velocity profile, with a slight decrease towards the walls. This matches what is seen in the experiments. Thus, SST $k-\omega$ is the model chosen to compute the simulations.

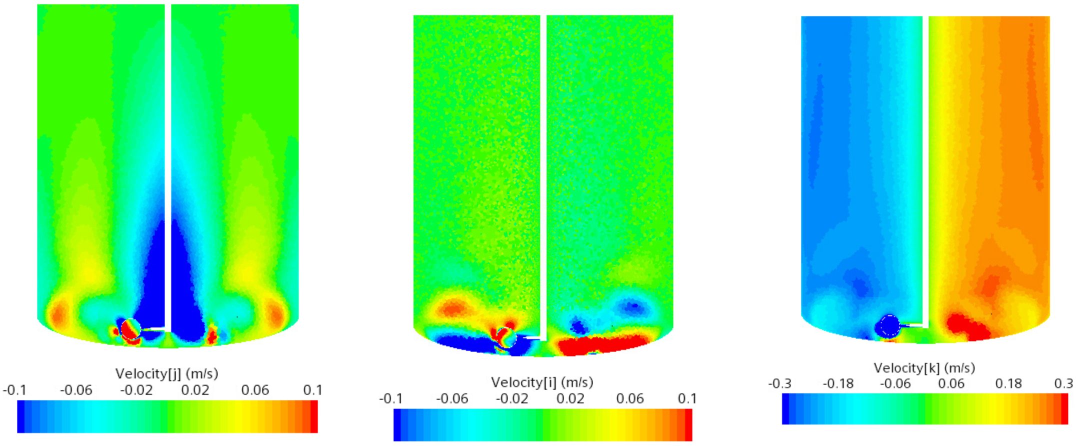

(a) Axial velocity. Real $k-\varepsilon$.

(b) Radial velocity. Real $k-\varepsilon$.

(c) Tangential velocity. Real $k-\varepsilon$.

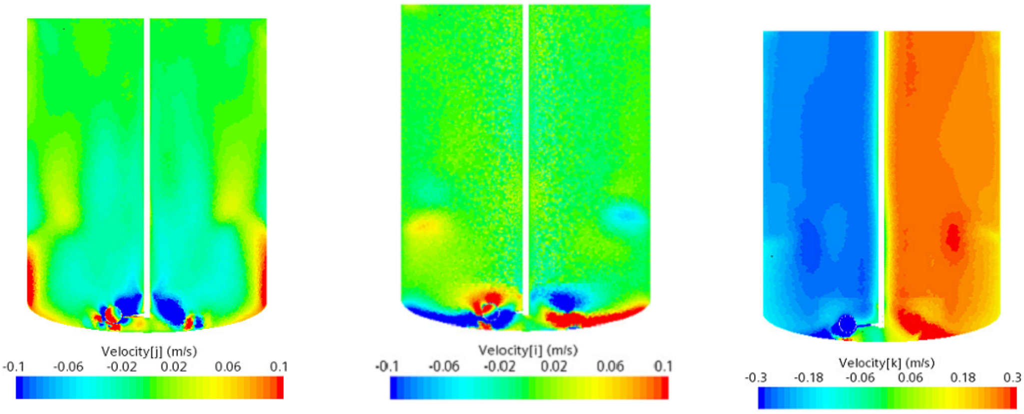

(d) Axial velocity. SST $k-\omega$.

(e) Radial velocity. SST $k-\omega$.

(f) Tangential velocity. SST $k-\omega$.

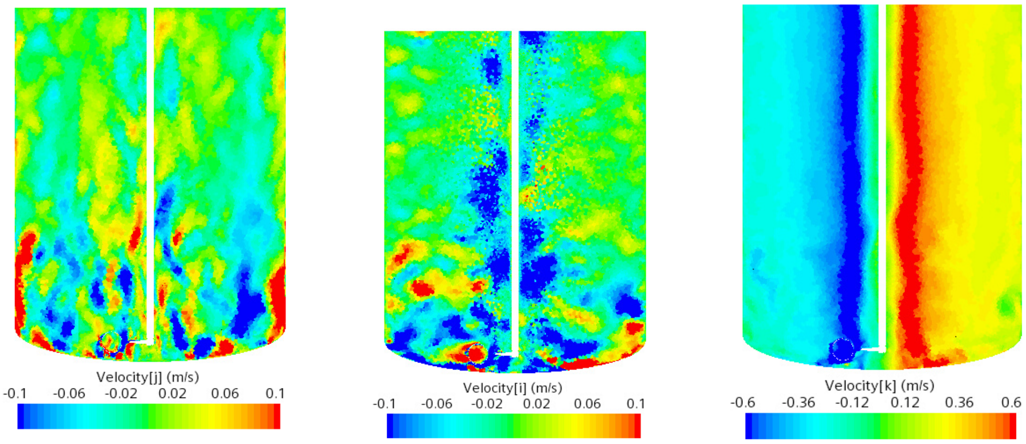

(g) Axial velocity. *LES*.

(h) Radial velocity. *LES*.

(i) Tangential velocity. *LES*.

Figure 4.4: Velocity fields for model comparisons.

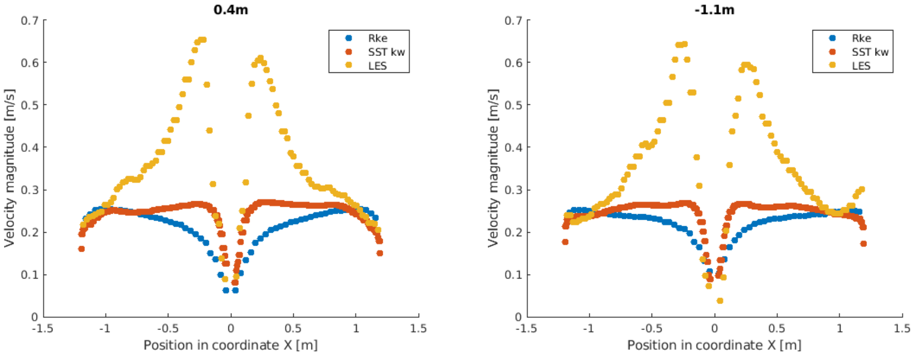

(a) Upper line. 2.8m.

(b) Mid-Upper line. 1.35m.

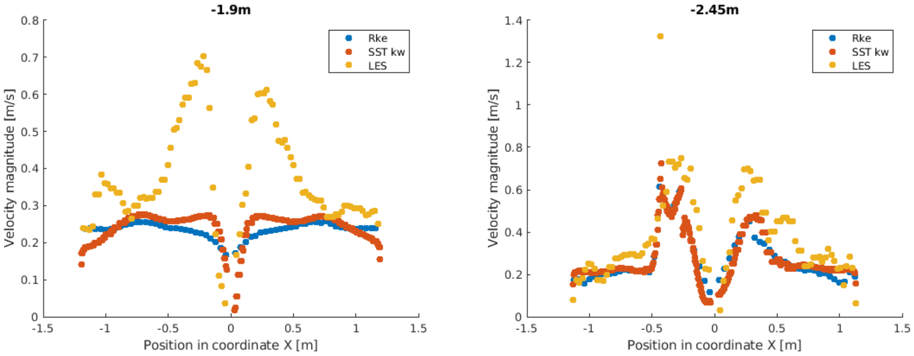

(c) Mid-bottom line. 0.55m

(d) Impellers-bottom line. 0 m,

Figure 4.5: Velocity magnitude along horizontal lines. Model sensitivity analysis.

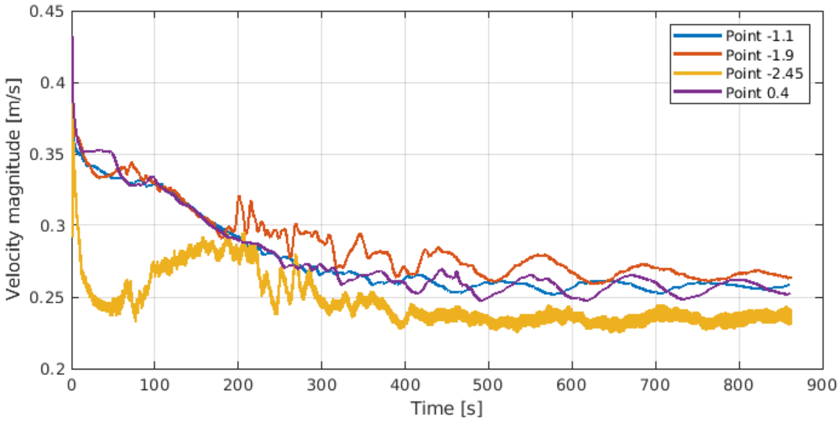

Figure 4.6: Evolution of velocity magnitude in the probe points.

4.2.1.3 SM predictions

The low overall movement together with the size of the tank and the stirrer placement, make the required time to stabilize the solution increase. In this case, the system takes up to $860s$ to reach an identified steady state, where the probe points of velocity show a visible periodicity with a constant average. At that moment, the fields of interest are extracted for a cross section of the tank, as seen in the previous section. The stabilization process in the velocity probe points explained in Section 3.2.6 can be seen in Figure 4.6. It can be seen how the velocities are decreased to a half from the original value of initialization, to then stabilize. The frequency content is also richer for the points close to the tank bottom, showing where the most turbulent regions are. A low-frequency unsteadiness seems to be present, due to the oscillation of the upper probes every $100s$ approximately.

Figure 4.4 depicts the stabilized velocity field solutions. Differences with the MRF prediction are visible. In this case, the radial field shows a discharge radial jet that impacts the wall and climbs upwards close to the wall. About half of the tank, the upward flow detaches from the wall and continues ascending to end up recirculating down in the central regions. Two small counter-vortices can be appreciated where the flow separates from the wall. The axial recirculation, however also shows that no vertical movement reaches the upper part of the tank. This is, of course, not promising for future particle distribution. As well, the radial movement for the vast majority of the fluid bulk is not existent. Bad radial and axial homogeneity is, therefore expected.

The tangential field (Figure 4.4f.) shows that the solid body rotation that MRF predicts (i.e. Figure 4.2c) has disappeared. Instead, the field shows a constant profile of velocities, where the speed is severely increased immediately after the shaft but stays in a plateau until some wall effects are encountered.

4.2.2 Particle distribution

After describing the flow fields, particles are introduced to investigate the predicted motion and their distribution. With these results, the homogeneity and cloud height can be yielded, according to the model predictions and compared with the experiments performed. To begin the calculations on a solid base, the solution from the transient seen in the previous sections, with the SST $k-\omega$ is used as initialization of the fields (i.e. Figure 4.4 second row). The settings described in Section 3.2.4 are used for these simulations. The particles are injected randomly in the domain with zero velocity.

4.2.2.1 1WC LPT

One-way coupled LPT is run at first. Particles are injected and the case continues running over the new initial SM solution[4]. Since the nature of this method ignores the effect of the particles on the flow, these fields are fast stabilized after the initialization, and the flow remains steady.

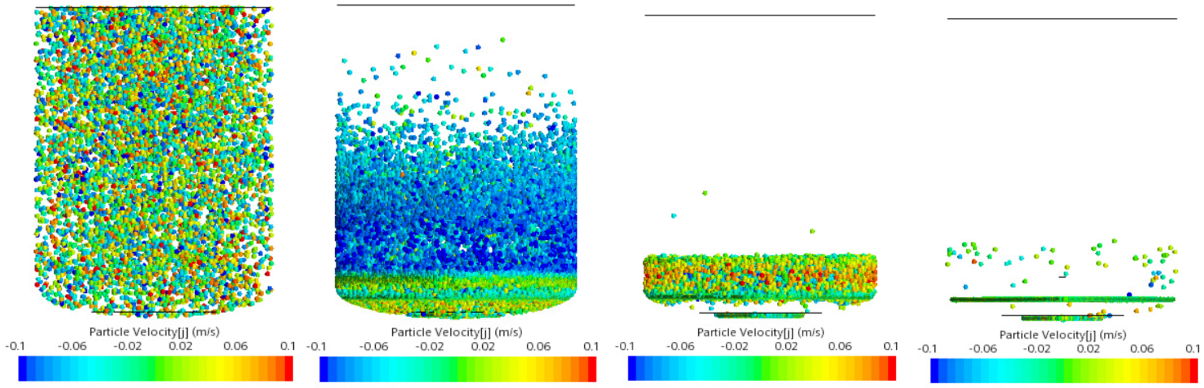

(a) Side. t=0s **(b)** Side. t=30s **(c)** Side. t=60s **(d)** Side. t=150s

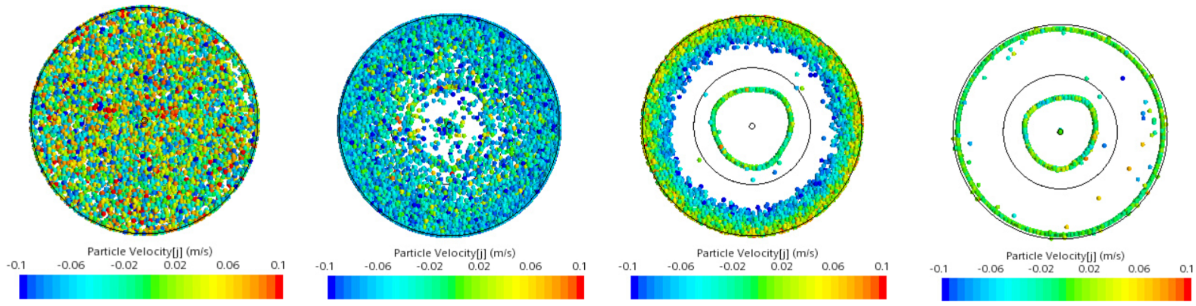

(e) Top. t=0s **(f)** Top. t=30s **(g)** Top. t=60s **(h)** Top. t=150s

Figure 4.7: 1WC-LPT. Particle evolution after injection.

The movement of the particles can be tracked in Figure 4.7[5]. Four snapshots can be seen where the state of the particles is described. From left to right, the simulation time increases. At first, the random injection can be appreciated since the particles have random velocities and are distributed across the whole domain. At that point, the flow fields must drive them towards their final destination, which is the main interest. After approximately 30s, the particles start to sink and at the same time a *ring* is forms, so the particles accumulate in the outer domain. This effect is increased with time, reaching at 60s a state where the particles form a *crown* around the impeller with low cloud height. A separation can be

---

[4] The one obtained from SM SST $k-\omega$ transient calculations.

[5] Particles are scaled for visualization reasons. The real particles are some orders smaller in size.

also observed from the top view, where some other particles are also accumulated in the cone trails in another and thinner ring. The final state, where the simulation is stopped, shows some particles slightly floating in the bottom third of the tank, while the vast majority is accumulated in two main rings. The first, the just mentioned in the cones tails, and the last, as a product of the also described *crown*, that has collapsed.

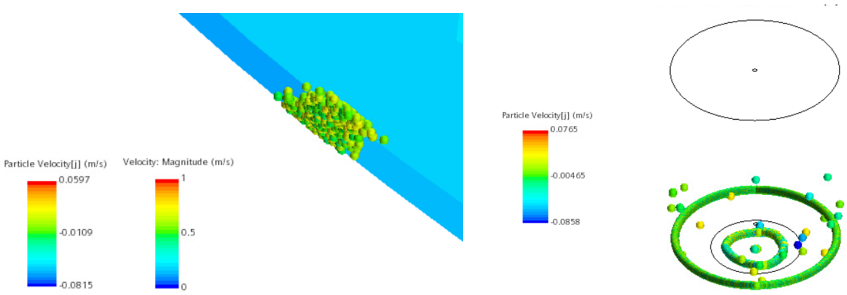

(a) VJ 1WC LPT. Zoom to the outer ring particle cluster.

(b) Isometric view

Figure 4.8: Clustering of particles in the tank bottom wall.

From that moment on, the particles cluster in that zone and never abandon the accumulation despite the simulation time, and remain swirling. This clustering is better described in Figure 4.8 where one zoom is seen in one of the bottom walls. As can be seen in Figure 4.8b. the predicted particle distribution is lousy, and no good cloud height, axial nor radial homogeneity is seen.

4.2.2.2 1WC DEM

Particle interactions are included in the simulations to observe if the clustering at the tank bottom is still yielded. The same initial solution is used for field initialization. With DEM simulations, new forces are active, as seen in 2.3.7. The settings used for these simulations are exposed in Table 3.6 where *Drag forces*, *Spin lift forces* are included in the simulations. The fields are initialized and a new unsteady simulation is run until no particle movement variation is appreciated.

The evolution of particle motion in the unsteady simulation can be followed in Figure 4.9. The same initialization as in the previous section is used, distributing thus the particles across the whole domain. There, is possible to see how at 0s, the tank is filled with particles evenly distributed through the tank. However, when the simulation time increases, the sinking is easily perceived. In Figure 4.9b, at t=25s, the particles accumulate themselves at the bottom third of the tank. That structure, is maintained in time, with the particles swirling, and also slowly sinking but in a pseudo-steady state. The radial distribution is also heavily affected with time. When focusing at the simulation end, the cones have discharged radially the flow in a way that most of the particles have been dragged to the walls, where these remain swirling.

On the other side, a clear cluster of particles is predicted in the cone trails and immediately below the shaft. This can be seen in the bottom row of Figure 4.9, especially in the right figure. These particles in a ring shape with a central dot, are immobile, as can be seen by its green color. When observing the velocity fields (i.e. Figure 4.4, second row) it can be seen that the flow does not affect heavily the space within the bottom clearance[6]. This lack of flow in that regions yields sedimentation of particles in that position.

In Figure 4.10 is clearly seen that the density of particles in the wall lifting regions is increased, compared

---

[6] Between the bottom wall and the impeller.

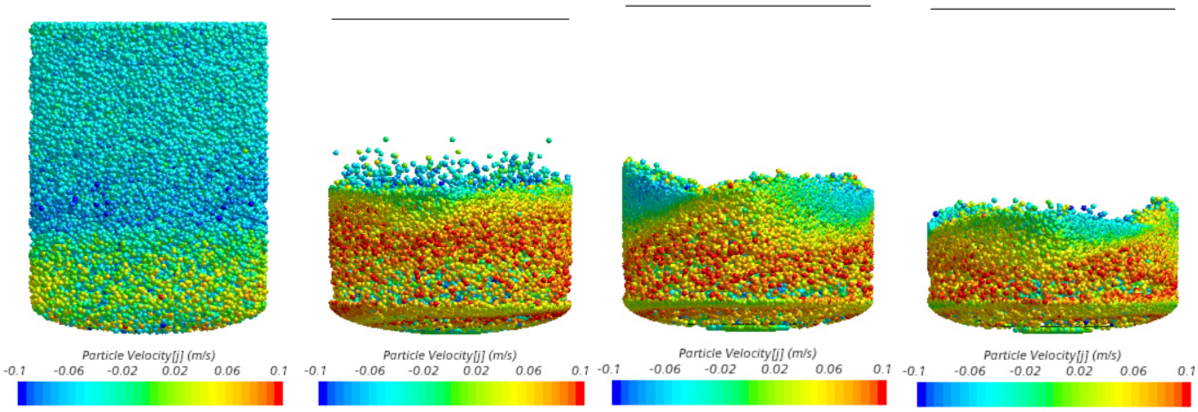

(a) Side. t=0s **(b)** Side. t=25s **(c)** Side. t=50s **(d)** Side. t=100s

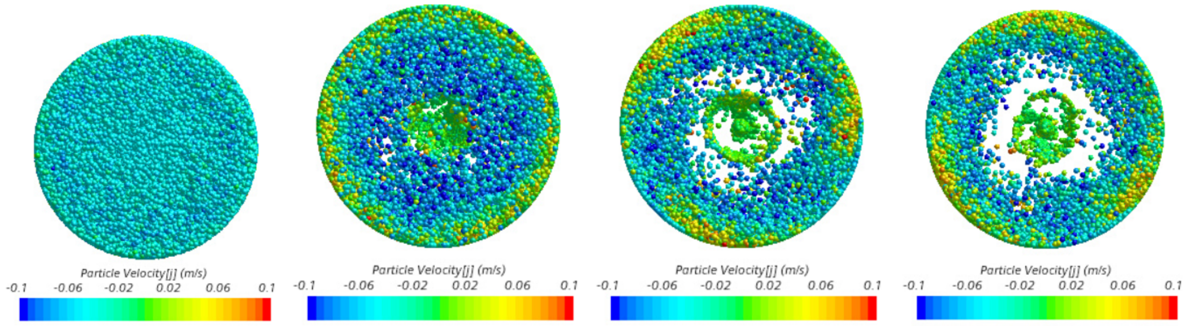

(e) Top. t=0s **(f)** Top. t=25s **(g)** Top. t=50s **(h)** Top. t=100s

Figure 4.9: 1WC-DEM. Particle evolution after injection.

to the 1WC-LPT case. No big clustering in the bottom wall is observed, and it seems to be solved by including the particle-particle interactions. In Figure 4.10b. can be seen how the particles recirculate in the tank. In simple terms, these lift close to the walls and then move downwards in another fluid layer also close to the outer domain. No particles are found in the central region, having a lousy radial uniformity.

4.3 ViscoJet validations

4.3.1 Homogeneity validation ViscoJet

In Section 4.1.2 it is seen that experiments are performed to measure the homogeneity of the mixing within the ViscoJet tank.

Since data is available both from experiments and from CFD simulations, a quick validation of the results is derived. Results from 1WC LPT and 1WC DEM are compared in Figure 4.11 with the experiments. This graphic shows the normalized mass concentration across the tank normalized volume. Figure 4.11 thus depicts that the particles are concentrated in the tank bottom, with no particles in the upper levels.

The simulation trends do not match correctly the experimental data. The accumulation of particles at the bottom is higher in the experiments than in simulations. The 1WC LPT simulation shows the peak of particle concentration around 10% of the volume. On the other side, 1WC DEM predicts lower peaks

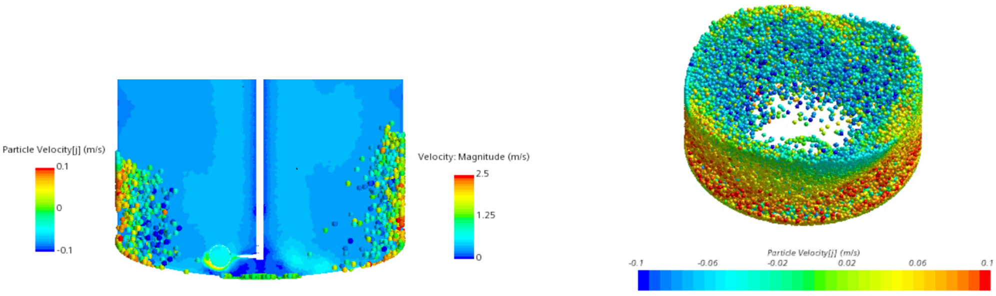

(a) Particle lifting in cross section.

(b) Recirculation of particles.

Figure 4.10: Particles in lifting regions.

but more distributed along the tank height. More tank height is thus, yielded with this method.

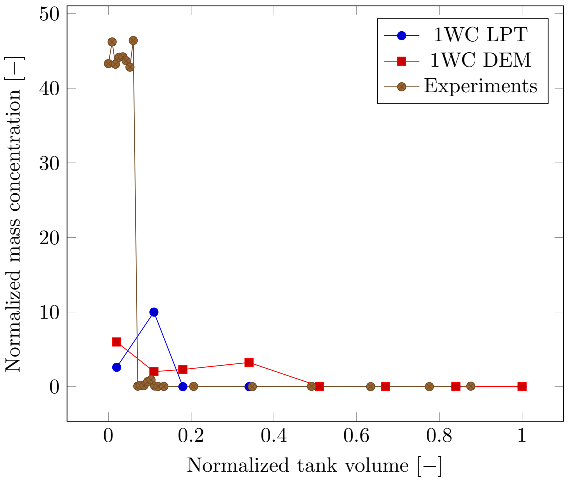

Figure 4.11: ViscoJet tank assessment. Particle concentration comparison.

Figure 4.11 gives then, the impression that 1WC-LPT models better the cloud height. However, there are discussions needed regarding that inference. On the first basis, the results shown by 1WC-LPT depicted in Figure 4.7 are rather unphysical and derived of the model limitations, due to its lack of particle interactions and physical mass of the particles. This creates clusters of particles that do not move, and completely ignore the lifting regions that the flow field provide. The fact that these results meet better the experimental trend is a coincidence due to the overall bad axial particle distribution. From what is seen in the predicted flow fields, a behavior such as the one predicted using DEM is more feasible.

One of the biggest drawbacks of this experimental validation is that, the homogeneity is being sampled in the tank by emptying it. Thus, both situations i.e. CFD and reality are not remotely identical. When emptying, different vortices may appear that could affect the steady behavior of the particles.

4.3.2 Visual validation

Comparing the video recordings with the obtained fields, it can be seen that the overall distribution of particles is correctly represented. In Figure 4.12, a comparison between experiments and simulations is depicted. Low axial mixing is appreciated, where all the particles concentrate at the tank bottom. The same way, a ring of particles can be found in the walls vicinity, with particle accumulation seemingly below the impeller cones. The height of particles, despite the recording point of view suggest that the cloud height is lower than the one predicted in Figure 4.9. The radial distribution is reasonably predicted using DEM.

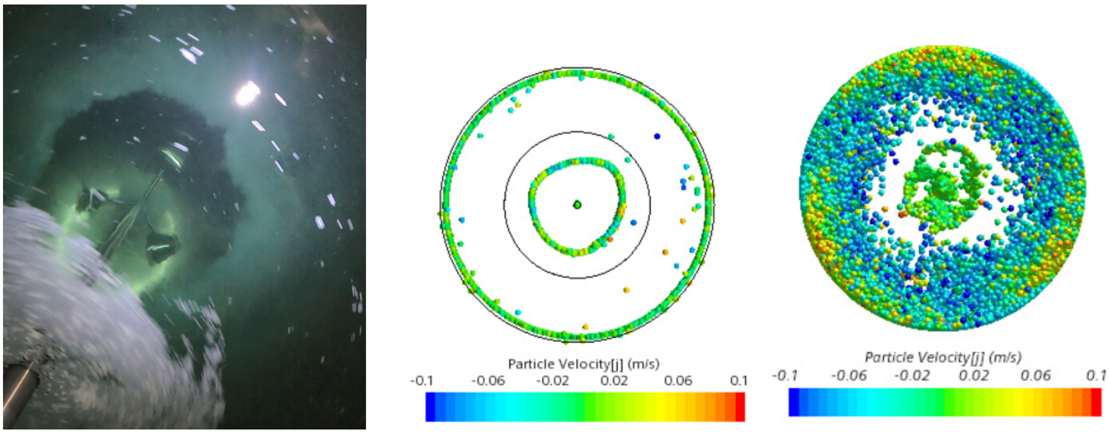

(a) Recording snapshot. **(b)** 1WC LPT. **(c)** 1WC DEM.

Figure 4.12: Visual validation of the ViscoJet tank.

4.4 Magnetic CFD results

4.4.1 Flow fields

The developed methodology is applied to the Magnetic tank, as well. Thus, a solution is obtained by using the steady MRF approach which is later used as a field initializer. Then, the motion modeling is changed and SM approach is used in order to carry a transient and more complex but accurate simulation. Furthermore, starting from the MRF solution saves computational time since the cells have values close to the real solution. Starting from the MRF solution, the transient is run until observable stabilization of the engineering variables (i.e. torque and velocity in probe points). Once this phenomenon appears, the simulation can be interpreted as converged and therefore finalized.

Interesting flow fields for future particle analysis are the velocity component fields. Since the stirrer is not located in a symmetrical location, the flow is not expected to be axisymmetric and therefore, the results are also analyzed in a perpendicular plane to the cross section.

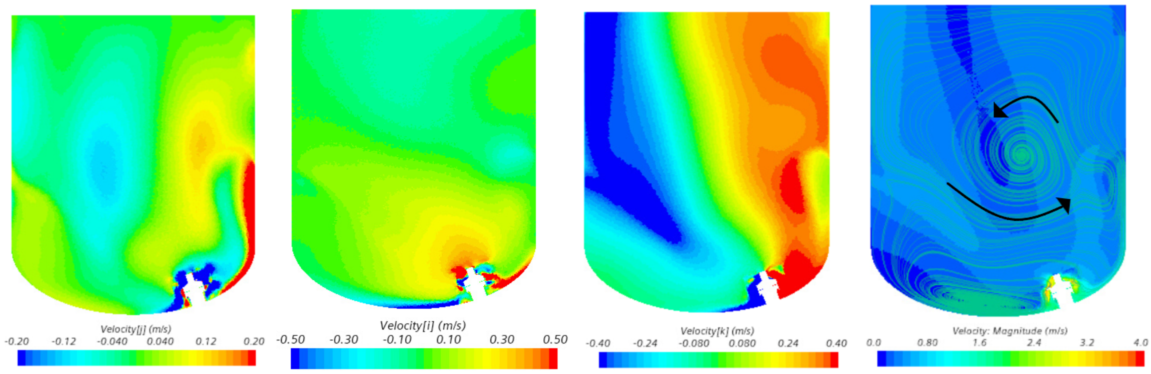

(a) Axial field. **(b)** Radial field. **(c)** Tangential field. **(d)** Magnitude.

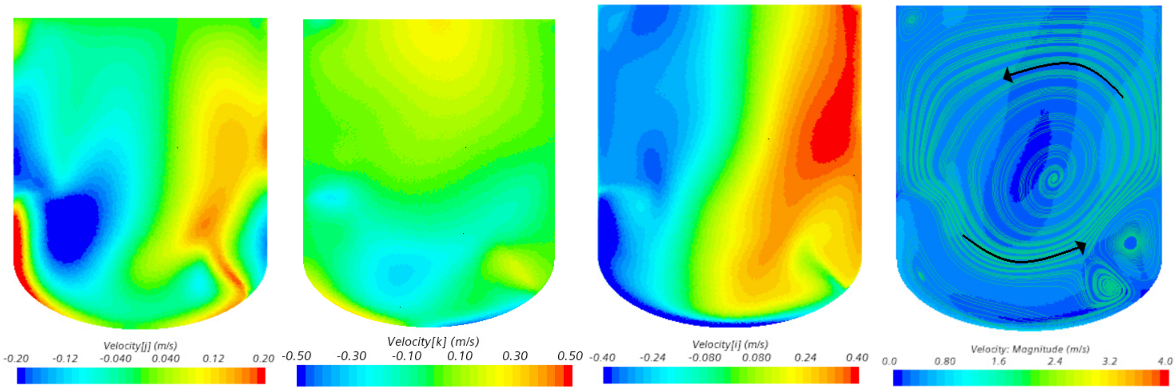

(e) Axial field. **(f)** Radial field. **(g)** Tangential field. **(h)** Magnitude.

Figure 4.13: MG SM snapshot steady results. Relevant velocity fields. First row, impeller plane. Second row, 90° section.

In Figure 4.13 the axial, radial, tangential and magnitude velocity fields are presented. The first row represents the cross section, that directly cuts through the impeller. The bottom row shows the perpendicular plane, in a way that the impeller is located between the observer and the plane (see Figure 3.15).

The axial component of the velocity shows how the impeller creates an important upwards flow in the right wall. Going up, the flow starts detaching from the wall, towards a clear central vortex. That way, part of the flow seems to rotate in that eddy whereas the other part recirculates down to the impeller. This named vortex can be seen in Figures 4.13 d, and h. In these, the velocity magnitude is represented but also streamlines are included to describe the flow different paths. Two sets of arrows mark the rotation direction of these vortices. From both of the planes, the big eddy is visible. Some other vortices exist, such as the one present in the cross section immediately beside the impeller forming a recirculation on its left hand side. This recirculation can be seen in 4.13b. where the impeller pushes part of the flow to the right wall, and part to the left side, recirculating. In the Side view (Figure 4.13h.), two little eddies are formed in the bottom right corner.

4.4.2 Particle fields

The solution present in Figure 4.13 is used as the starting point for the particle simulations. 70.000 particles are injected in a random set of points alongside the whole domain.Both LPT and DEM are run to understand the difference in predictions and evaluate the accuracy of each method.

4.4.2.1 1WC LPT

The settings for this simulations are exposed in Section 3.3.5. To understand the particle behavior, different snapshots of the particle position transient are presented in Figure 4.14. The axial velocity is chosen as the scalar field so the pictures represent if the particles are moving upwards or downwards. To visualize the domain, frontal and superior snapshots are provided for every time selected. This way, the axial and radial distribution can be evaluated visually.

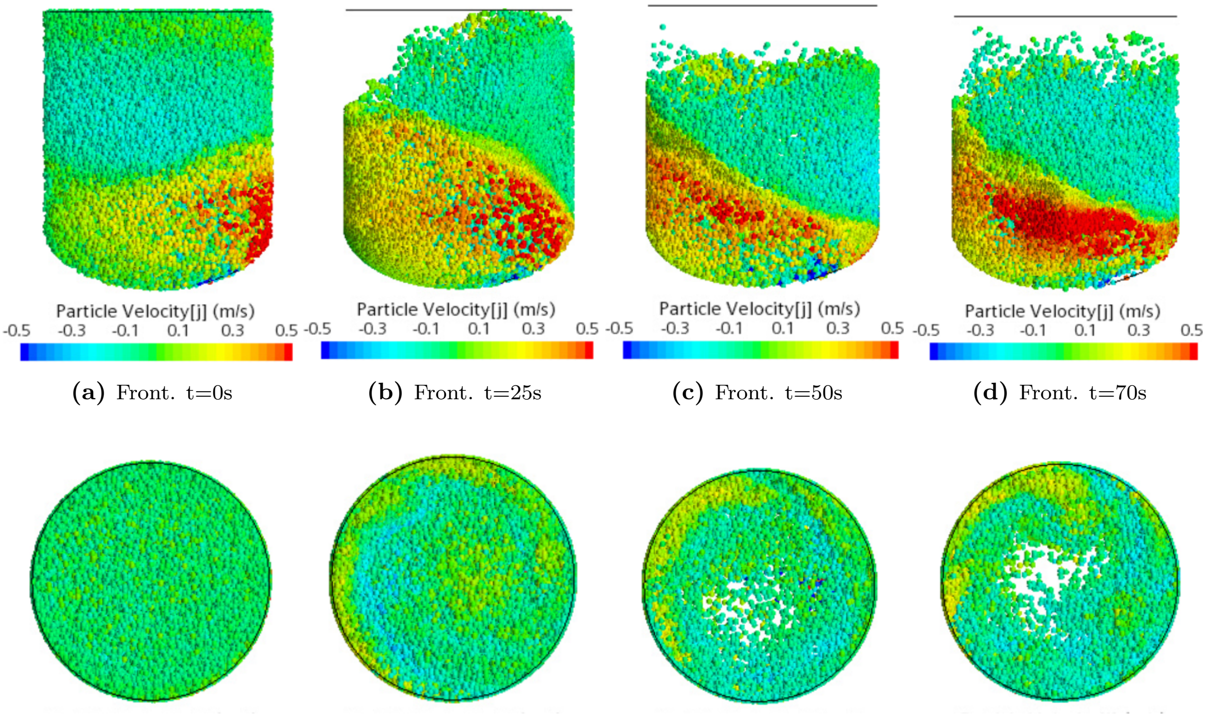

(a) Front. t=0s **(b)** Front. t=25s **(c)** Front. t=50s **(d)** Front. t=70s

(e) Top. t=0s **(f)** Top. t=25s **(g)** Top. t=50s **(h)** Top. t=70s

Figure 4.14: MG 1WC LPT results. Particle evolution.

The first set of pictures on the left show the state of the particles a timestep after its injection. It is possible to see how these particles have adopted some of the velocity that the flow possesses. The particles seem radially and axially evenly distributed. A general lifting zone appears on the right wall, since the particles are being carried by the discharge flow that the impeller provides. Then, these impinge on the wall and move axially. When the time increases, some particles start to sink and accumulate at the bottom. The cloud height is reduced (see Figures 4.14c. and d.) but the predictions do not show a drastic loss in axial distribution. The lifting particles seem to move during the simulation from the right wall, diagonally to the left wall almost forming a 45º line. This is induced by the combined effect of the lifting and the strong rotation that the impeller creates. The radial distribution is worsened with time. The impeller action drives the majority of the particles near the walls and, when seeing Figure 4.14h. an empty region is visible from top to bottom.

4.4.2.2 1WC DEM

Particle interactions are accounted for DEM simulations. New forces as shear lift, spin lift and drag forces are computed to take into account collisions both within particles and with the walls. The SM stabilized solution is used as the simulation starting point. As in the other simulations, 70.000 particles are injected randomly and evenly in the domain. A transient simulation is computed until particles adopt their steady movement. The particle evolution can be seen in four different snapshots in Figure 4.15. Frontal and superior views are presented so the majority of the domain is visible. The figure represents the axial movements of the particles with yellow/red colors meaning lifting and blue colors being sinking.

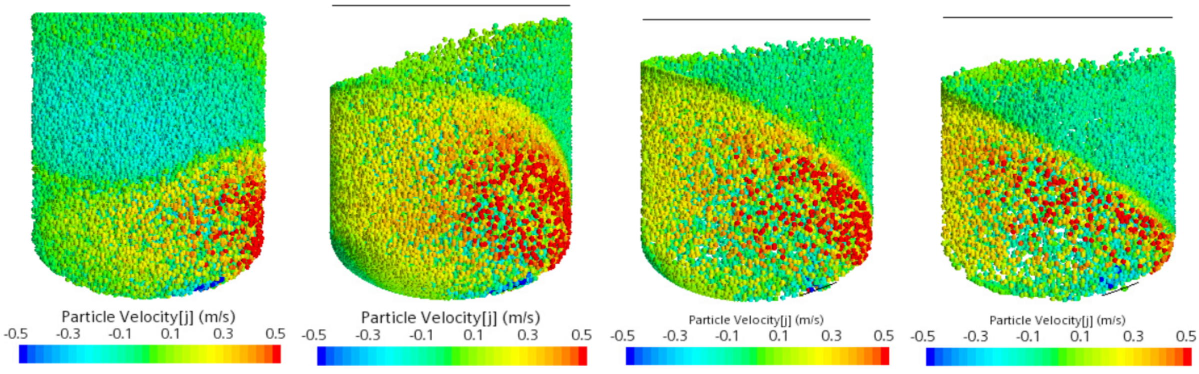

(a) Front. t=0s **(b)** Front. t=25s **(c)** Front. t=50s **(d)** Front. t=100s

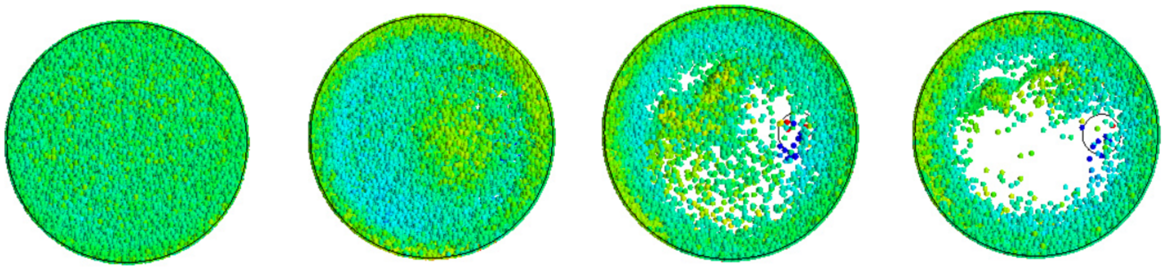

(e) Top. t=0s **(f)** Top. t=25s **(g)** Top. t=50s **(h)** Top. t=100s

Figure 4.15: MG 1WC DEM Magnetic results. Particle evolution.

After the injection, the particles are evenly distributed both radially and axially. A vortex is formed in the middle of the tank. As seen in Figure 4.14 the lifting of particles starts on the right side of the tank, where the impeller is located to then form a 45º lifting region. The domain seems to be divided in two by the mentioned diagonal. When focusing on the superior view, the sinking and radial movement of the particles towards the wall is visible. The predicted radial distribution seems worsened when using DEM than when using LPT. Particle accumulations at the bottom are seen, in bigger magnitudes to what is seen in LPT simulations (see Figure 4.14).

To see better this particle lump at the tank bottom, Figure 4.16 is depicted. Using the velocity magnitude as the scalar field, the particles have almost no motion when their color is dark blue. Four snapshots of different simulation times are provided. When observing the accumulation evolution, one can say that its position is constant, but the quantity of particles accumulated is time-dependent. This is probably caused because the particles start to accumulate until the group increases its volume and it can be suctioned by the impeller flow.

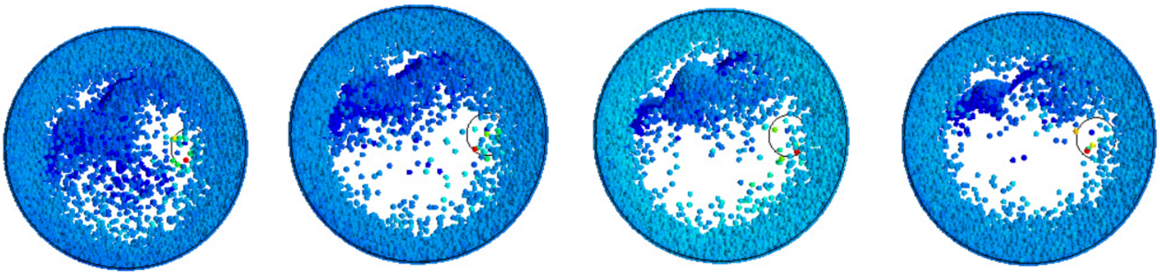

(a) t=50s **(b)** t=65s **(c)** t=75s **(d)** t=100s

Figure 4.16: MG 1WC DEM. Accumulation of particles in the bottom.

4.5 Magnetic validations

4.5.1 Homogeneity validation Magnetic tank

Figure 4.17 depicts the normalized mass concentration across the tank volume. Both the simulations and experiments seem to match relatively well. The number of samples of the experiments is substantially higher and thus, more detailed. However, for each simulation sample its respective experimental sample is reasonably close. The presence of particles in the upper levels is always higher in the simulations.

Despite the trend match, the results show a high deviation from the uniform suspension. In the lower volumes, the concentration is 10 times higher, whereas in the upper ones, particles cannot almost be found.

4.5.2 Visual validations

Figure 4.18 depicts a comparison between the video recordings of the Magnetic tank, and the obtained results. It can be observed that in the recordings, a remarkable accumulation of particles is present in the left side of the picture. This accumulation was predicted by 1WC DEM simulations (see Figure 4.16), but missed when using LPT.

However, the accumulation is not correct in DEM also. The figures have been aligned so the stirrer is placed in the same approximated position. The accumulation is less dense in the simulations, and closer to the impeller, than what is shown in the movies. This is a complicated problem to solve since it incorporates accumulation of particles, and therefore, apart from particle-particle interactions, the particle-fluid interactions should also be computed. This will require the usage of 2WC, that will allow the fluid to be conscious about the particle presence, instead of the actual solution, where the fluid simply

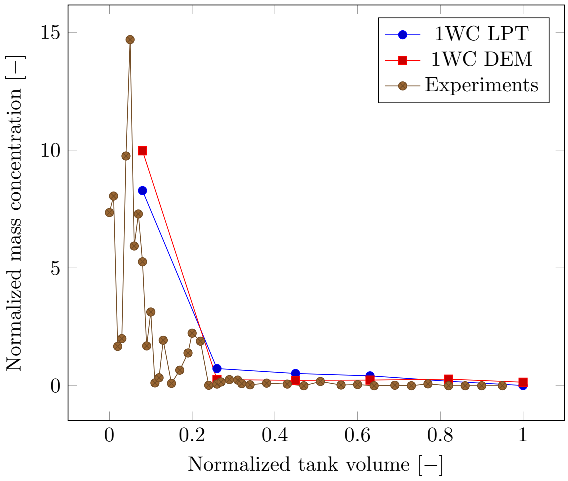

Figure 4.17: Magnetic tank assessment. Particle concentration comparison.

goes through them. Setting up a 2WC simulation is more demanding computationally, since the time required per iteration is higher.

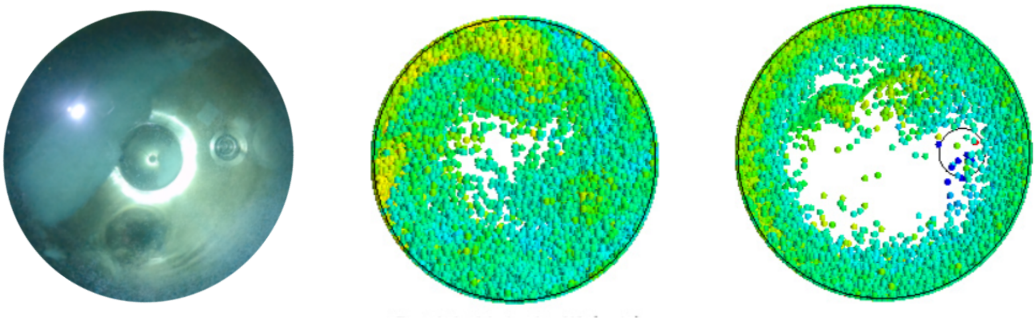

(a) Recording snapshot. **(b)** 1WC LPT. **(c)** 1WC DEM.

Figure 4.18: Visual validation of the Magnetic tank.

Chapter 5

Assessment of the stirrers performance

In this section, the performance of the two tanks are discussed. This discussion is based on how the mixing could be performed, depending on the quality of the flow fields and the overall results of particle simulations.

A comparison can only be established when the input power in known for both tanks. At equal input power, the best stirrer is the one that achieves better solid suspension uniformity.

Table 5.1 shows the calculated power number for both of the stirrers, according to equation (2.1).

Table 5.1: Calculated power number for both stirrers.

	ViscoJet	**Magnetic**
Power number [-]	0.65	0.20
Tank Reynolds number [-]	450000	700000

The power number from the ViscoJet stirrer is approximately 3 times higher. Thus, the magnetic stirrer shows a lower power consumption, and the results analyzed in the assessment must consider it.

5.1 Flow fields

The ViscoJet equipped tank shows flow fields with strong tangential velocity component dominance. The axial movement is limited to the bottom half of the tank, with the important motion located in the bottom third. The radial component shows a jet that impinges the wall when discharged radially. Two recirculation vortices are located at impeller height, and little counter vortices close to the tank half. The lack of experimental probes, due to the complexity of this measurements in a real sized tank, together with the turbulence model divergence, leads to uncertainty of the flow field predictions.

Opposed to this, the magnetic stirrer creates in the tank a more dynamic and turbulent flow. The overall velocities show higher magnitudes, and the motion is more significant. The flow seems to move rotationally around the walls, with the creation of one big vortex in the tank center, and multiple subvortices of smaller size in the tank corners.

These vortices can potentially create good solid suspension, since the radial and axial recirculations are enhanced.

5.2 Particle fields

Particle analysis in both of the tanks show that both of them show poor solid suspension uniformity.

The ViscoJet, as seen in the flow fields, concentrates all the particles in the bottom, close to the walls. The magnetic, yields more cloud height, since some particles are able to reach higher altitudes, carried by the strong flow stream that the impeller creates. However, both of them yield unsatisfactory results in radial distributions, since the particles are pushed towards the walls, and no good recirculations in radial direction seem to appear.

The performance compared of this two mixers can be seen in Figure 5.1[1], where the different data analyzed for both of the stirrers is faced. In the mentioned Figure, the first thing that can be noticed is that for the ViscoJet predictions, the particles seem to be more concentrated in the bottom. As seen, experiments and VJ 1WC LPT predict all the particles below, 15%. VJ 1WC DEM around 30% (i.e. bottom third of the tank). Nonetheless, MG calculations predict particle distribution in the higher volumes. Note that the normalized mass concentration is not zero in the upper volumes for this tank. This directly yields that the axial homogeneity of the Magnetic equipped tank is better, as depicted directly from the presented snapshots[2].

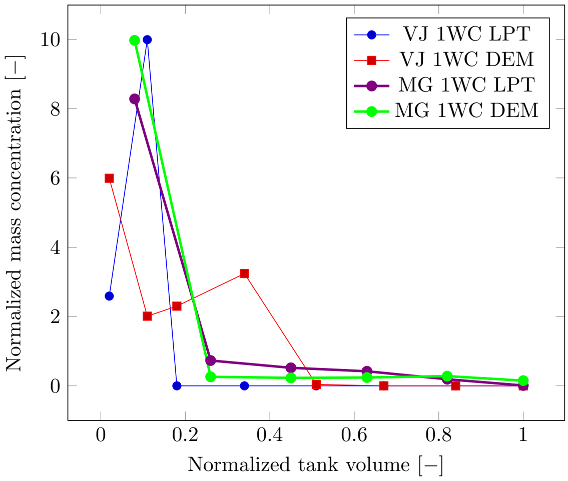

Figure 5.1: Normalized particle concentration in tanks comparison.

Thus, despite the difference in power consumption seen in Table 5.1, the Magnetic stirrer yields better results. Both flow fields and particle predictions present conditions that theoretically can enhance the solid suspension uniformity. The ViscoJet on the other side, presents discouraging results from an engineering point of view.

However, it must be remarked that both of the distributions are poor, and peaks that high of the normalized curves are undesired, i.e. values should be around 1. The uniformity levels seen need to be improved, and the change in rotational speed, or the stirrer placement can be the first decisions to take.

---

[1] Experimental data here not depicted for line clarity. If needed consult Figures 4.11 and 4.17.

[2] Compare Figure 4.9 with Figure 4.15.

Chapter 6

Conclusions

In this project, a CFD methodology to simulate flow fields with particles is developed and used in two tank-stirrer geometries. For the correct modelling of the flow fields, the RANS SST-$k-\omega$ turbulence model is used, offering good results. The methodology uses the MRF approach to calculate a first inital solution, used afterwards to run a transient case using SM. This combination of approaches allow a fast and accurate result, able to capture existing periodicities in the flow. To use this method, the domain of the tank is divided in two, a stationary and a spinning region. This project has shown how an incorrect definition of regions leads to unphysical results. It has been concluded that a good practice is to keep the spinning region close to the impeller, where there is substantial flow movement (see Appendix B).

The selected turbulence model has worked correctly in both of the tank-stirrer combinations. Visual validations on the free surface for the ViscoJet case suggest that this model stands out over other models such as Realizable $k-\varepsilon$ or LES. However, one must remark that the conditions in which LES is run in this thesis are not ideal, and a more refined mesh should be used close to the impellers.

To simulate particles, a set of methodologies has been evaluated as well. This thesis has focused in 1WC simulations, therefore not including particles effect on the fluid. Both of the tanks were analyzed using LPT and DEM methodologies. Comparing with experimental recordings, is possible to say that both of them match relatively well the real particle distribution. The particles move towards the locations seen in the experimental data. DEM has proven to be more physical, since LPT produces substantial clusterings in some of the cases. Including the particle-particle interactions is suggested when the overall level of suspension is low and thus the particle sediment. However, both of the tested methodologies over-predict the cloud height, compared to what is seen in the experiments. More research is needed to solve this issue.

The stirrer interactions with the flow have also been analyzed. The centered ViscoJet causes an agitation that resembles a Rushton turbine. The flow is discharged radially and low recirculation is obtained. The cones do not show remarkable results and no good lifting is observed due to their action. On the other side, the Magnetic stirrer geometry and speed creates better flow motion, that forms important recirculation vortices, especially a centered one, that affects the majority of the tank. These vortices could lead to good mixing that has not been otherwise observed in the analysis. Different experiments could be performed to set a more suitable rotation speed.

Understanding these interactions allowed an assessment of the stirrers. Both of the stirrers, with these configurations, offer lousy results. The distribution of particles is not efficient, since these are not spread axially and radially throughout the tank. When compared, the magnetic stirrer presents more potential, since the flow fields create the above-mentioned vortices and overall bigger bottom-to-top movement, enhanced also by its placement in the tank. Research is needed to obtain better configurations for these stirrers to be used.

Chapter 7

Future work

Regarding the developed methodology to predict the flow fields with particles, there are different lines to move forward. It is seen in that the flow field predictions present an important dependence on the turbulence model. Thus, it is of high importance to fully determine if the turbulence model chosen is the most accurate. Floating particles could be released in the liquid surface and let them swirl. By correctly identifying the surface flow, different turbulence models can be discarded. A similar procedure of validation has been performed in this thesis, but the accuracy can be heavily improved. An extra-value that should be measured is the torque. This is an easy parameter to measure electronically and can help discerning between turbulence models. Furthermore, if possible, some probes could be located within the tank, to capture velocity-time series that can be compared with simulations. For the particle distribution prediction, several other aspects need to be assessed. Experimental data shows for both of the tanks lower cloud heights than simulation predictions. This, is increased when using DEM. An evaluation of how the particle-particle interaction is performed can be of high utility. Several coefficients that affect the particle-particle interactions can be researched. These could be tuned to correctly simulate the real particle behavior. On the other side, particle accumulations and lumps are seen, specially in the Magnetic tank using 1WC-DEM. Whilst this behavior is correctly predicted according to the experimental recordings, the shape and steadiness was though, not matching. The above-mentioned particle-particle modeling can affect this accumulation behavior. However, when dealing with aggregations of particles of this caliber, the 2WC option needs to be assessed. Lumps of particles can affect considerably the surrounding flow behavior and thus, this approach can play a key role in the predictions.

Finally, some considerations must be made regarding the results offered by the stirrers assessment. The ViscoJet presents poor results due to the flow fields that it creates. Numerous reasons could be behind this lousy results, and these could be assessed in the future. The actual impeller placement is more that unadvised, since it is located too low in the tank. Thus, different impeller placements could be tested, beginning with a clearance increase. If the emptying is then strongly compromised, different configurations can be considered such as stacking another impeller in the shaft. This would allow a low clearance in the first impeller whose lack of recirculations is supplemented by the secondary impeller. The Magnetic stirrer on the other side, delivers correct flow fields. The high rotational speed pushes strongly the particles towards the walls. Different speeds could be tested, to tune the best behavior. As well, the particle lump is undesired. Different impeller placement could be tested to decrease this effect.

Bibliography

[1] *The dairy processing handbook. Tetra Pak.* 2021. URL: `https://dairyprocessinghandbook.tetrapak.com/chapter/tanks`.

[2] J.Y. Oldshue. *Fluid Mixing Technology.* McGraw-Hill Chemical Engineering Series. Chemical Engineering, 1983. ISBN: 9780076067145. URL: `https://books.google.se/books?id=qL70UjG3bZQC`.

[3] David S. Dickey. *Mixing and blending.* Kirk-Othmer Encyclopedia of Chemical Technology, 2010.

[4] Jim Gregory and Katy Lentz. *Vortex breakers in Practice - Chemical Engineering.* 2016. URL: `https://www.chemengonline.com/vortex-breakers-practice/`.

[5] E.L. Paul, V.A. Atiemo-Obeng, and S.M. Kresta. *Handbook of Industrial Mixing: Science and Practice.* Wiley, 2004. ISBN: 9780471451440. URL: `https://books.google.se/books?id=s4SsrmvEc7QC`.

[6] Song Zhiyao et al. "A simple formula for predicting settling velocity of sediment particles". In: *Water Science and Engineering* 1.1 (2008), pp. 37–43. ISSN: 1674-2370. DOI: `https://doi.org/10.1016/S1674-2370(15)30017-X`. URL: `https://www.sciencedirect.com/science/article/pii/S167423701530017X`.

[7] H.K. Versteeg and W. Malalasekera. *An Introduction to Computational Fluid Dynamics: The Finite Volume Method.* Pearson Education Limited, 2007. ISBN: 9780131274983. URL: `https://books.google.se/books?id=RvBZ-UMpGzIC`.

[8] F. White. *Fluid Mechanics.* McGraw-Hill series in mechanical engineering. McGraw-Hill Higher Education, 2015. ISBN: 9781259165924. URL: `https://books.google.se/books?id=NqpZCgAAQBAJ`.

[9] Yoshihide Tominaga. "Flow around a high-rise building using steady and unsteady RANS CFD: Effect of large-scale fluctuations on the velocity statistics". In: *Journal of Wind Engineering and Industrial Aerodynamics* 142 (2015), pp. 93–103. ISSN: 0167-6105. DOI: `https://doi.org/10.1016/j.jweia.2015.03.013`. URL: `https://www.sciencedirect.com/science/article/pii/S0167610515000732`.

[10] *RANS models.* 2021. URL: `https://docs.sw.siemens.com/documentation/external/PL20191230144651718/en-US/userManual/userGuide/html/index.html#page/STARCCMP/GUID-235E939A-BC77-4988-AE0A-D79B17FD6072.html`.

[11] S.B. Pope. *Turbulent Flows.* Cambridge University Press, 2000. ISBN: 9781139643351. URL: `https://books.google.se/books?id=4rghAwAAQBAJ`.

[12] W.P Jones and B.E Launder. "The prediction of laminarization with a two-equation model of turbulence". In: *International Journal of Heat and Mass Transfer* 15.2 (1972), pp. 301–314. ISSN: 0017-9310. DOI: `https://doi.org/10.1016/0017-9310(72)90076-2`. URL: `https://www.sciencedirect.com/science/article/pii/0017931072900762`.

[13] *Realizable k-Epsilon model.* 2009. URL: `https://www.afs.enea.it/project/neptunius/docs/fluent/html/th/node60.html`.

[14] David C. Wilcox. "Formulation of the k-w Turbulence Model Revisited". In: *AIAA Journal* 46.11 (2008), pp. 2823–2838. DOI: `10.2514/1.36541`. eprint: `https://doi.org/10.2514/1.36541`. URL: `https://doi.org/10.2514/1.36541`.

[15] *SST k-Omega model formulation.* 2011. URL: `https://www.cfd-online.com/Wiki/SST_k-omega_model`.

[16] *Curvature correction factor in Star-CCM+.* 2021. URL: `https://docs.sw.siemens.com/documentation/external/PL20200227072959152/en-US/userManual/userGuide/html/index.html#page/STARCCMP%5C%2FGUID-254F222E-9F83-421B-8FFE-E73C18C3EBDA.html%5C%23`.

[17] *LES model.* 2021. URL: `https://docs.sw.siemens.com/documentation/external/PL20200227072959152/en-US/userManual/userGuide/html/index.html#page/STARCCMP%5C%2FGUID-FAA8C83A-F618-4E59-8BF9-486BEE191EB6.html%5C%23`.

[18] J. SMAGORINSKY. "GENERAL CIRCULATION EXPERIMENTS WITH THE PRIMITIVE EQUATIONS: I. THE BASIC EXPERIMENT". In: *Monthly Weather Review* 91.3 (1963), pp. 99–164. DOI: `10.1175/1520-0493(1963)091<0099:GCEWTP>2.3.CO;2`. URL: `https://journals.ametsoc.org/view/journals/mwre/91/3/1520-0493_1963_091_0099_gcewtp_2_3_co_2.xml`.

[19] M. Germano et al. "A dynamic subgrid-scale eddy viscosity model". In: *Physics of Fluids* 3 (1990), pp. 1760–1765.

[20] Harminder Singh, David F. Fletcher, and Justin J. Nijdam. "An assessment of different turbulence models for predicting flow in a baffled tank stirred with a Rushton turbine". In: *Chemical Engineering Science* 66.23 (2011), pp. 5976–5988. ISSN: 0009-2509. DOI: `https://doi.org/10.1016/j.ces.2011.08.018`. URL: `https://www.sciencedirect.com/science/article/pii/S0009250911005720`.

[21] Madhavi Sardeshpande and Vivek Ranade. "Computational fluid dynamics modelling of solid suspension in stirred tanks". In: *Current Science* 102 (June 2012).

[22] G.R. Kasat et al. "CFD simulation of liquid-phase mixing in solid–liquid stirred reactor". In: *Chemical Engineering Science* 63.15 (2008), pp. 3877–3885. ISSN: 0009-2509. DOI: `https://doi.org/10.1016/j.ces.2008.04.018`. URL: `https://www.sciencedirect.com/science/article/pii/S0009250908001929`.

[23] Aoyi Ochieng and Alison E. Lewis. "CFD simulation of solids off-bottom suspension and cloud height". In: *Hydrometallurgy* 82.1 (2006), pp. 1–12. ISSN: 0304-386X. DOI: `https://doi.org/10.1016/j.hydromet.2005.11.004`. URL: `https://www.sciencedirect.com/science/article/pii/S0304386X06000028`.

[24] A. Tamburini et al. "CFD simulations of dense solid–liquid suspensions in baffled stirred tanks: Prediction of the minimum impeller speed for complete suspension". In: *Chemical Engineering Journal* 193-194 (2012), pp. 234–255. ISSN: 1385-8947. DOI: `https://doi.org/10.1016/j.cej.2012.04.044`. URL: `https://www.sciencedirect.com/science/article/pii/S1385894712005062`.

[25] Aljaz Janic. "CFD Simulation of Particles in Pipe Flow and Mixing Tank". MA thesis. Linköping University, Applied Thermodynamics and Fluid Mechanics, 2020, p. 70.

[26] Oskar Lundström and Henrik Syrjä. *Study of Particle Homogeneity in Mixing Tanks Using Experiments and CFD*. eng. Student Paper. 2021.

[27] *MRF in Star-CCM+*. 2021. URL: `https://docs.sw.siemens.com/documentation/external/PL20200227072959152/en-US/userManual/userGuide/html/index.html#page/STARCCMP%5C%2FGUID-94D66D5B-010A-4809-83E0-591648C56F47.html%5C%23wwID0E3TRFB`.

[28] *SM in Star-CCM+*. 2021. URL: `https://docs.sw.siemens.com/documentation/external/PL20200227072959152/en-US/userManual/userGuide/html/index.html#page/STARCCMP%5C%2FGUID-E41FCF0D-765F-449A-80A6-D981EE023BBB.html%5C%23`.

[29] *Conservation of equations with Mesh Motion in Star-CCM+*. 2021. URL: `https://docs.sw.siemens.com/documentation/external/PL20200805113346338/en-US/userManual/userguide/html/index.html?param=X3PDy&authLoc=https://thesteveportal.plm.automation.siemens.com/AuthoriseRedirect#page/STARCCMP%5C%2FGUID-49B8F0BB-3AD6-47F5-B25B-01C061AA6276.html%5C%23wwID0EB62UD`.

[30] Anne de Lamotte et al. “Identifying dominant spatial and time characteristics of flow dynamics within free-surface baffled stirred-tanks from CFD simulations”. In: *Chemical Engineering Science* 192 (2018), pp. 128–142. ISSN: 0009-2509. DOI: `https://doi.org/10.1016/j.ces.2018.07.024`. URL: `https://www.sciencedirect.com/science/article/pii/S0009250918304950`.

[31] Deyin Gu et al. “Numerical investigation on mixing characteristics of floating and sinking particles in a stirred tank with fractal impellers”. In: *Journal of the Taiwan Institute of Chemical Engineers* 116 (2020), pp. 51–61. ISSN: 1876-1070. DOI: `https://doi.org/10.1016/j.jtice.2020.11.013`. URL: `https://www.sciencedirect.com/science/article/pii/S1876107020303540`.

[32] Divyamaan Wadnerkar et al. “CFD simulation of solid–liquid stirred tanks”. In: *Advanced Powder Technology* 23.4 (2012). Special Issue Featuring Articles from Chemeca 2011, pp. 445–453. ISSN: 0921-8831. DOI: `https://doi.org/10.1016/j.apt.2012.03.007`. URL: `https://www.sciencedirect.com/science/article/pii/S0921883112000386`.

[33] Ameur H. et al. Foukrach M. Bouzit M. “Effect of Agitator’s Types on the Hydrodynamic Flow in an Agitated Tank”. In: (2020). DOI: `https://doi.org/10.1186/s10033-020-00454-2`.

[34] *Multiphase flows in Star-CCM+*. 2021. URL: `https://docs.sw.siemens.com/documentation/external/PL20200227072959152/en-US/userManual/userGuide/html/index.html#page/STARCCMP%5C%2FGUID-40F39626-68FC-4928-9695-77394F6B83D8.html%5C%23`.

[35] *Eulerian-Eulerian models in Star-CCM+*. 2021. URL: `https://docs.sw.siemens.com/documentation/external/PL20200227072959152/en-US/userManual/userGuide/html/index.html#page/STARCCMP%5C%2FGUID-EE4D4F81-7DE4-4529-A9CE-150314BF8ACB.html%5C%23wwID0EACH1B`.

[36] *Eulerian-Lagrangian models in Star-CCM+*. 2021. URL: `https://docs.sw.siemens.com/documentation/external/PL20200227072959152/en-US/userManual/userGuide/html/index.html#page/STARCCMP%5C%2FGUID-AD4497B4-33A5-4874-B0F7-E3EB762CDB5D.html%5C%23wwconnect_header`.

[37] *2 Way Coupling in Star-CCM+*. 2021. URL: `https://docs.sw.siemens.com/documentation/external/PL20200227072959152/en-US/userManual/userGuide/html/index.html#page/STARCCMP%5C%2FGUID-BD6FE61B-6EEB-40B6-AC94-757E475707BA.html%5C%23`.

[38] *VISCO JET® Agitation Systems*. 2021. URL: `https://www.viscojet.com/en/contact/`.

[39] *Particle equations in Star-CCM+*. 2021. URL: `https://docs.sw.siemens.com/documentation/external/PL20200227072959152/en-US/userManual/userGuide/html/index.html#page/STARCCMP%5C%2FGUID-1CAF3A65-9203-4AFF-8316-70CBEA981BDB.html%5C%23`.

[40] *Cpntact force in Star-CCM+*. 2021. URL: https://docs.sw.siemens.com/documentation/external/PL20200805113346338/en-US/userManual/userguide/html/index.html?param=X3PDy&authLoc=https://thesteveportal.plm.automation.siemens.com/AuthoriseRedirect#page/STARCCMP%5C%2FGUID-D9FD8743-D2A9-4705-87AF-BB88B9BDDA58.html.

Appendices

Chapter A

Particle forces

Here, the forces that act on the particle, seen in Section 2.3.7 are detailed.

Drag force

The drag forces is defined as in equation (A.1) where C_d is the drag coefficient, ρ_s is the density of the particle and $v_s = v - v_p$ is the particle slip velocity [39].

$$F_d = \frac{1}{2} C_d \rho_s A_p |v_s| v_s \tag{A.1}$$

The calculation of C_D has different models regarding the Reynolds number of the particle. In Section 2.3.7 one of these correlations was explained, where the C_D had different expression for every turbulent regime.

One correlation wide used as well for spherical solid particles is the Schiller-Naumann correlation (Equation (A.2)).

$$C_d = \begin{cases} \frac{24}{Re_p}\left(1 + 0.15 Re_p^{0.684}\right) & Re_p \leq 1000 \\ 0.44 & Re_p > 1000 \end{cases} \tag{A.2}$$

Pressure gradient force

The pressure gradient force is defined as in equation (A.3), where V_p is the volume of the particle and ∇p_{static} is the gradient of the static pressure in the continuous phase.

$$\mathbf{F}_p = -V_p \nabla p_{static} \tag{A.3}$$

Virtual Mass Force

The virtual mass force is calculated by:

$$\mathbf{F}_{vm} = C_{vm}\rho V_p \left(\frac{D\mathbf{v}}{Dt} - \frac{d\mathbf{v}_p}{dt} \right) \tag{A.4}$$

where C_{vm} is the virtual mass coefficient.

Gravity Force

The gravitational force is obtained with:

$$\mathbf{F}_g = m_p \mathbf{g} \tag{A.5}$$

where g is the gravitational constant.

Spin Lift Force

This force affects to a particle that spins relatively to a fluid. The velocity differential between the particle opposite sides due to rotation, causes a pressure differential.

$$F_{LR} = \frac{\rho\pi}{8} D_p^2 C_{LR} |\mathbf{v}_s| \frac{\mathbf{\Omega} \times \mathbf{v}_s}{|\mathbf{\Omega}|} \tag{A.6}$$

where Ω is the relative angular velocity of the particle to the fluid C_{LR} is the coefficient of rotational lift calculated with (Sommerfield):

$$C_{LR} = 0.45 + \left(\frac{Re_R}{Re_p} - 0.45 \right) e^{-0.5684 Re_R^{0.4} Re_p^{0.3}} \tag{A.7}$$

Shear Lift Force

The velocity gradient in the continuous phase creates a pressure distribution on the particle, yielding the shear lift force. The force is defined as:

$$F_{LR} = \frac{\rho\pi}{8} D_p^3 C_{LS} (\mathbf{v}_s \times \omega) \tag{A.8}$$

where C_{LS} is the shear lift coefficient (Sommerfield) and ω is the curl of the fluid velocity. Sommerfield shear lift coefficient can be calculates as:

$$C_{LS} = \frac{4.1126}{Re_S^{0.5}} f(Re_p, Re_S) \tag{A.9}$$

where $f(Re_p, Re_S)$ us a function of the particle and shear flow Reynolds numbers.

Contact Force

The contact force is typically computed using a spring-damper model. The spring accounts for the repulsive force of the collision whereas the damping allows the modeling of particles not perfectly elastic.¨As Figure A.1 depicts, two spring-damper models at the contact point, one representing the tangential force and the other the normal one.

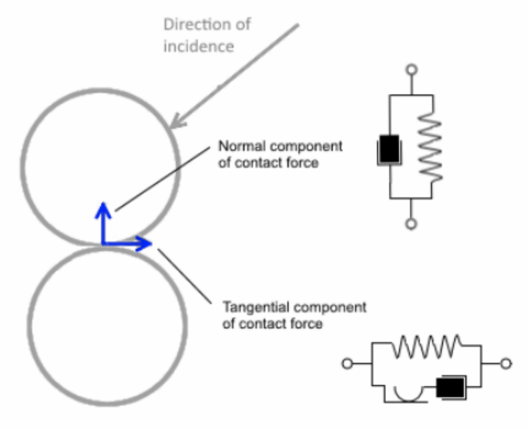

Figure A.1: Modeling of the contact force.

Different contact models exist, using in this thesis the Hertz Mindlin one [40]. The forces between two spheres are described using:

$$\mathbf{F}_C = F_n\mathbf{n} + F_f\mathbf{t} \tag{A.10}$$

where, F_n and F_t are the magnitudes of the normal and tangential forces. The normal direction is defined by a normal force (F_n) a normal spring stiffness (K_n) and a normal damping (N_n). The respective expressions follow:

$$F_n = -K_n d_n - N_n v_n \tag{A.11}$$

$$\begin{aligned} K_n &= \frac{4}{3}E_{eq}\sqrt{d_n R_{eq}} \\ N_n &= \sqrt{(5K_n M_{eq})}N_{n,damp} \end{aligned} \tag{A.12}$$

On the other side, the tangential force is determined by its homonyms parameters.

$$Ft = \begin{cases} -K_t d_t - N_t v_t, & if|K_t d_t| < |K_n d_n|C_{fs} \\ \dfrac{|K_n d_n C_{fs} d_t|}{|d_t|} & otherwise \end{cases} \tag{A.13}$$

$$K_t = 8G_{eq}\sqrt{d_t R_{eq}} \tag{A.14}$$

$$N_t = \sqrt{(5K_t M_{eq})}N_{t,damp} \tag{A.15}$$

The expressions for $N_{n,damp}$ and $N_{n,damp}$ follow:

$$N_{n,damp} = \frac{-ln(C_{n,rest})}{\sqrt{\pi^2 + ln(C_{n,rest}^2}} \tag{A.16}$$

$$N_{t,damp} = \frac{-ln(C_{t,rest})}{\sqrt{\pi^2 + ln(C_{t,rest}^2}} \tag{A.17}$$

In here, $C_{n,rest}$ and $Ct, rest$ are the normal and tangential coefficients of restitution. This parameters are tuned by the user.

Finally, some equivalent parameters for the physical properties of the particles are defined.

$$R_{eq} = \frac{1}{\dfrac{1}{R_A} + \dfrac{1}{R_B}} \tag{A.18}$$

$$M_{eq} = \frac{1}{\dfrac{1}{M_A} + \dfrac{1}{M_B}} \tag{A.19}$$

$$E_{eq} = \frac{1}{\dfrac{1-{\nu_A}^2}{E_A} + \dfrac{1-{\nu_B}^2}{E_B}} \tag{A.20}$$

$$E_{eq} = \frac{1}{\dfrac{2(2-\nu_A)(1+\nu_A)}{E_A} + \dfrac{2(2-\nu_B)(1+\nu_B)}{E_B}} \tag{A.21}$$

where:

- M_A M_B, are masses of sphere A and B.
- d_n and d_t are overlaps in the normal and tangential direction at the contact.
- R_A and R_B are the particles radius.
- E_A and E_B are the Young's modulus of the particles.
- ν_A and ν_b are the Poisson's ratios.
- ν_n and ν_t are the normal and tangential velocity components of the relative sphere surface velocity at the contact point.

Chapter B

Modeling the spinning region

A first approach was used and later discarded, where the spinning region was modeled using a cylinder that enclosed the stirrer and the whole shaft. As mentioned, the motion was set to the commented region, so the complete cylinder spins the mesh according to the specified rotation.

The transient using SM is run until steady and the velocity contour plots are obtained. These are exposed in Figure B.1. The axial field show radial jets traveling from the cones to the walls and then moving axially upwards until two-thirds of the tank height. From that point, it recirculates down in the center bulk. The radial contour plot shows two main vortices in the tank bottom, enclosing the cones, whereas different counter vortices can also be seen in the top recirculation zones.

However, this model is discarded soon in the research due to the predictions that the tangential field is showing. A clear jump in between regions exists, where the spinning region shows close to zero motion of the bulk. This is an unphysical result since no such difference in speed can exist when crossing the interface that separates both domains. This interface is merely a mathematical entity and should transfer correctly the flow motion.

This miscalculation in the fields also affected variables such as the torque, wherein Figure B.2 shows a higher absolute value, when compared with the chosen approach. This is due the high-pressure gradient that exists between the inside flow of the cone and the outside zero velocity prediction.

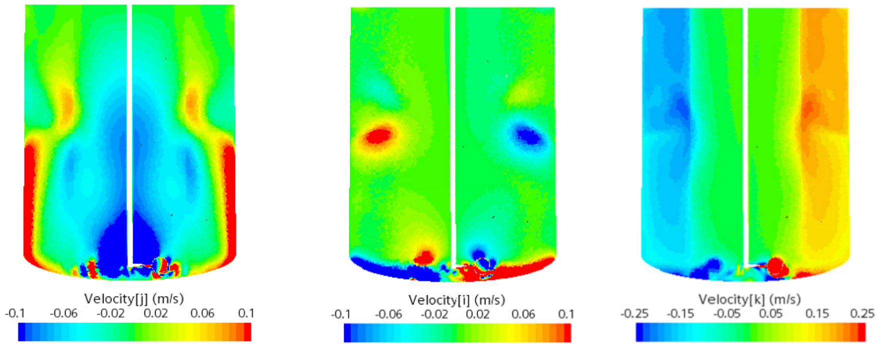

(a) Axial velocity field. **(b)** Radial velocity field. **(c)** Tangential velocity field.

Figure B.1: Transient results for the first modeling method.

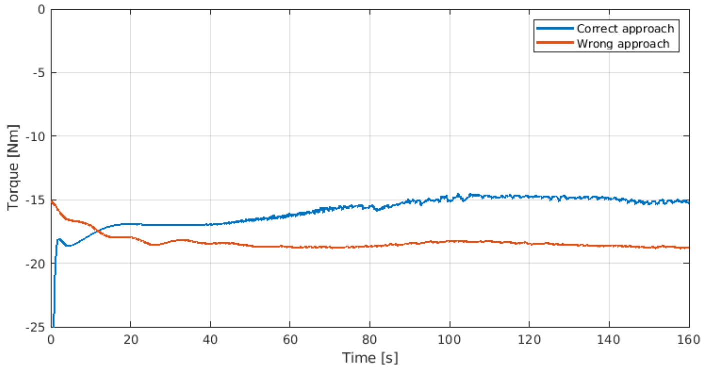

Figure B.2: Torque with the wrong modeling approach.

Chapter C

Experimental data

C.1 Settling velocity measurements

The particles are released in the fluid surface of the bucket. The sinking time is measured and the settling velocity is calculated. Results of the experiment can be seen in Table C.1. Figure C.1 depicts the samples taken with the respective standard deviation.

Table C.1: Experimental measurements of the particle settling velocity.

Height [m]	**Time** [s]	**Velocity** [m/s]
0.093	1.88	0.049
0.093	1.44	0.065
0.093	1.37	0.068
0.093	1.59	0.058
0.093	1.39	0.067
0.093	1.72	0.054
0.093	1.43	0.065
0.093	1.16	0.080
0.093	1.72	0.054
0.093	1.4	0.066
0.093	1.74	0.053
0.093	1.45	0.064
0.093	1.73	0.054
0.093	1.77	0.053
	Average	**0.061**

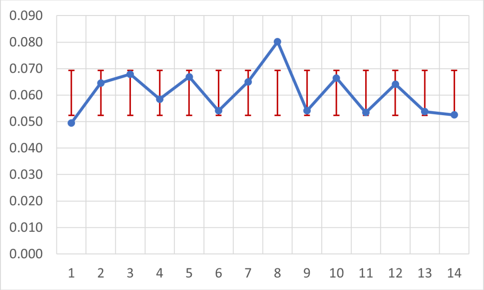

Figure C.1: Data samples and standard deviation.

C.2 Free surface particle analysis

Here the particle length analysis in the surface can be seen. This is used to determine empirically the velocity field in the free surface layer and its proximities. Particles are sampled in length in two different radius depicted in Figure C.2. The length of the particles depend on the camera shutter speed, and the particle velocity. 20 samples are taken and the data is shown in Table C.2. Figure C.3 shows the length distribution and the standard deviation of the measures.

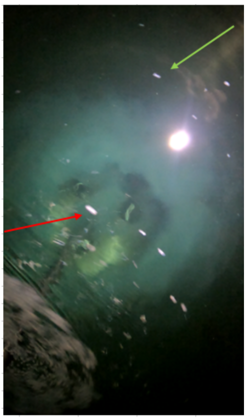

Figure C.2: Measurements of particles length on the free surface. Distance 1, inner radius (red). Distance 2, outer radius (green).

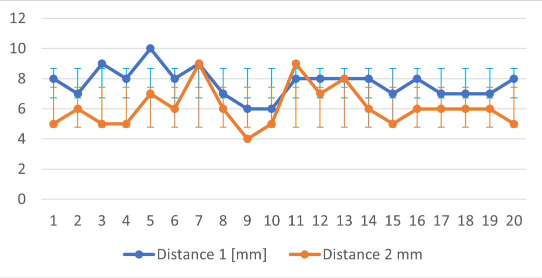

Figure C.3: Samples of particles length on the free surface.

Table C.2: Model sensitivity analysis. Length of particles in the free surface.

Sample **-**	**Distance 1** **[mm]**	**Distance 2** **mm**
1	8	5
2	7	6
3	9	5
4	8	5
5	10	7
6	8	6
7	9	9
8	7	6
9	6	4
10	6	5
11	8	9
12	8	7
13	8	8
14	8	6
15	7	5
16	8	6
17	7	6
18	7	6
19	7	6
20	8	5
Average	**7.7**	**6.1**
SDEV	**0.95**	**1.3**